This is the peer-reviewed, final accepted version for American Mineralogist, published by the Mineralogical Society of America.
The published version is subject to change. Cite as Authors (Year) Title. American Mineralogist, in press.
DOI: https://doi.org/10.2138/am-2022-8515. http://www.minsocam.org/

Revision 2

High-pressure behavior of 3.65 Å phase: Insights from Raman spectroscopy

Abhisek Basu[1,*], Mainak Mookherjee[1], Christelle Bucag[1], Sergey Tkachev[2], Bernd Wunder[3]

[1]Earth Materials Laboratory, Earth, Ocean and Atmospheric Science, Florida State University, Tallahassee, Florida 32306, USA

[2]Center for Advanced Radiation Sources, University of Chicago, Chicago, Illinois 60637, USA

[3]Deutsches GeoForschungsZentrum GFZ, Section 3.6, Telegrafenberg, 14473 Potsdam, Germany

*abasu@fsu.edu

ABSTRACT

The 3.65 Å phase ($MgSi(OH)_6$) is a hydrous phase that is predicted to be stable in a simplified MgO-SiO_2-H_2O (MSH) ternary system at pressures exceeding 9 GPa. Along cold subduction zones, it is likely to transport water, bound in its crystalline lattice, into the Earth's interior. The 3.65 Å phase consists of Mg and Si octahedral sites attached to the hydroxyl group that forms a hydrogen bond and is predicted to undergo pressure-induced symmetrization of the hydrogen bond. Therefore, in this study, we investigate the high-pressure behavior of the 3.65 Å phase using Raman spectroscopy. We have conducted five distinct compressions up to ~60 GPa using two different pressure transmitting media – alcohol mixture and neon. At ambient conditions, we identified vibrational modes using complementary first-principles simulations based on density functional perturbation theory. Upon compression, we note that the first derivative of the

vibrational modes in the lattice region stiffens, i.e., $b_i^{lattice} > 0$. In contrast, the hydroxyl region softens, i.e., $b_i^{OH} < 0$. This is indicative of the strengthening of hydrogen bonding upon compression. We noticed a significant broadening of vibrational modes related to hydroxyl groups that are indicative of proton disorder. However, within the maximum pressures explored in this study, we did not find evidence for pressure-induced symmetrization of the hydrogen bonds. We used the pressure derivative of the vibrational modes to determine the ratio of the bulk moduli and their pressure derivative. We note that the smaller bulk moduli of hydrous phases compared to the major mantle phases are compensated by significantly larger pressure derivatives of the bulk moduli for the hydrous phases. This leads to a significant reduction in the elasticity contrast between hydrous and major mantle phases. Consequently, the detection of the degree of mantle hydration is likely to be challenging at greater depths.

KEYWORDS: Subduction zone, Hydrous Mineral Phases, 3.65 Å phase, high-pressure Raman spectroscopy, diamond anvil cell (DAC), hydrogen bonding.

INTRODUCTION

Water exerts a significant influence on the dynamics of the solid Earth. For instance, water is known to lower melting temperatures (Hirschmann 2006) and affects transport properties including the rheology of the mantle (Karato 2010). Thus, considerable research has been done to understand how water is transported into the deep Earth and how much water is stored in the deep Earth. The efficiency of the transport of water is related to the thermodynamic stability of mineral phases including hydrous minerals and nominally anhydrous minerals. It is well known that hydrous phases often have limited thermal stabilities and hence they tend to dehydrate releasing water. The released aqueous fluids affect the surrounding mantle which eventually leads to the melting of the overlying mantle wedge and is known to trigger earthquakes (Iwamori 1998, 2004, 2007; Kawamoto 2006). However, a part of the water is retained in dense hydrous phases which are efficient in transporting water to greater depths. Hence, significant research has been conducted to quantify the phase stabilities of hydrous phases (Kawamoto 2006; Pawley et al. 2011). Recent experimental studies on the simplified ternary system for hydrated mantle lithosphere, i.e., the MgO-SiO_2-H_2O (MSH) system have documented the existence of 3.65 Å phase – a thermodynamically stable form of $MgSi(OH)_6$ with a structure characterized by lattice plane spacing of 3.65 Å (Wunder et al. 2011, 2012; Koch-Müller et al. 2021) at pressures of 9-10 GPa. This phase is formed from the breakdown of the 10 Å phase ($Mg_3Si_4O_{10}(OH)_2.nH_2O$) (Pawley et al. 2011; Wunder et al. 2011, 2012; Koch-Müller et al. 2021). The 3.65 Å phase could potentially transport ~35 wt% water, bound in its crystalline lattice, into the deep interior.

How much water is efficiently transported and sequestered in the deep Earth can be better understood if we can map the degree of mantle hydration. Thus it is crucial to have better

constraints on the elastic and transport properties of these hydrous phases and nominally anhydrous phases and relate these constraints on the physical properties of the mineral aggregates with the geophysical observables. A key issue is that these hydrous phases often have high compressibility than that of nominally anhydrous phases, and it is quite important to have a better understanding of how pressure and temperature affect the atomistic structure and which in turn influences the physical properties of these minerals. Most of the hydrous phases are characterized by hydrogen bonding, which, upon compression may evolve to a pressure-induced symmetrization. This often leads to significant changes in physical properties including elasticity such that the properties of hydrous phases could become indistinguishable from that of the bulk of the mantle, i.e., nominally anhydrous phases (Tsuchiya et al. 2002, 2005).

Recent first-principles simulations on the 3.65 Å phase have predicted the hydroxyl (OH) bond length (d_{OH}) to increase and the corresponding ($d_{O\ldots O}$) distance to shorten considerably under compression eventually resulting in a hydrogen bond-symmetrization at pressures ~60 GPa (Mookherjee et al. 2015). Hydrogen-bond symmetrization occurs when the hydrogen atom in an ($O-H\ldots O$) unit is located exactly at the center of the ($d_{O\ldots O}$) unit, i.e., ($d_{OH}=\frac{1}{2}d_{O\ldots O}$). Several, hydrogen-bearing mineral phases have been predicted to undergo similar hydrogen-bond symmetrization including δ-AlOOH , β-CrOOH, phase-D, phase H, and phase-Egg. For instance, δ-AlOOH undergoes symmetrization at ~16-24 GPa (Panero and Stixrude 2004; Sano-Furukawa et al. 2008) and β-CrOOH undergoes symmetrization at ~5 GPa (Jahn et al. 2012), and Phase-D undergoes symmetrization at ~40 GPa (Tsuchiya et al. 2002). However, many of these studies are based on theoretical predictions and the predicted symmetrization pressures often differ from the experimental observations. For instance, a vibrational spectroscopic study

on phase-D indicated the symmetrization to occur at a higher pressure (Shieh et al. 2009). So, it is important to test the theoretical predictions through high-pressure experiments.

In this study, we explore the high-pressure behavior of the 3.65 Å phase using Raman spectroscopy with particular emphasis on the evolution of the hydroxyl stretching to understand pressure-induced changes in hydrogen bonding. In addition, we also explore the pressure evolution of the low-wavenumber modes to provide a better constraint on the ratio of bulk modulus and its pressure derivative.

METHODS

The sample of 3.65 Å-phase studied was synthesized at 10 GPa and 425 ^{o}C (Wunder et al. 2011). The peak pressure and temperature were held for 77 hours in a multi-anvil apparatus at GeoForschungsZentrum, Potsdam, Germany. The synthesized material was characterized using electron microprobe analysis to confirm the stoichiometry of the 3.65 Å phase as $MgSi(OH)_6$. Powder X-ray diffraction confirmed the structure of the synthesized 3.65 Å phase. The details of the synthesis and the characterization have been reported in earlier studies (Wunder et al. 2011, 2012).

In this study, we explored the high-pressure behavior of the 3.65 Å phase using Raman spectroscopy. The Raman spectra were acquired in a Horiba Jobin Yvon LabRam Evolution spectrometer at the Earth Materials Laboratory, Florida State University. The spectrometer has a backscattering configuration and is equipped with a grating of 1800 lines/mm with a resolution of ~2 cm^{-1}. The spectrometer is also equipped with a thermoelectrically cooled CCD detector, an Olympus 50X long working distance infinity-corrected objective. We employed a frequency-doubled Nd-YAG laser (λ =532 nm) with a 300 mW maximum output power at the source.

It is well known that hydrous mineral phases often have limited thermal stability and are likely to be sensitive to the power of the laser. In a recent study, an incremental increase of laser power resulted in incremental heating of the hydrous mineral sample within the diamond anvil cell (Basu and Mookherjee 2021). Thus, we explored the effect of laser power on the 3.65 Å phase by increasing the laser power in incremental steps of 10, 25, 50, and 100% (of 300 mW at the source) and collected Raman spectra at ambient conditions. We repeated the stepwise increase of laser power to evaluate the effect of laser power on the sample within the diamond anvil cell with the cell closed by its weight, i.e., without any static compression. Upon incrementally increasing the laser power, for the 3.65 Å, we did not observe any identifiable changes in the mode frequency position of the hydroxyl stretching region, 2800-3500 cm^{-1} (Supporting Figure SF1). However, we optimized the laser power and exposure time to minimize the possibility of damaging the sample from over-exposure and local laser heating. To obtain a good signal-to-noise ratio we acquired Raman spectra of the 3.65 Å phase in the spectral range 100-1250 cm^{-1} with an acquisition time of 60 s and 10 accumulations and in the range 2850-3600 cm^{-1} with an acquisition time of 30 s and 10 accumulations.

We compressed powdered 3.65 Å phase to high pressures in a symmetric diamond anvil cell (DAC). The DAC was fitted with two low fluorescence type Ia diamond anvils. Each anvil had 300 μm diameter culets. We used a stainless-steel foil of 150 μm thickness as the gasket material. We pre-indented the foil to 50 μm thickness. A sample chamber hole of 100 μm diameter was drilled using a Boehler-Almax micro-driller. We conducted five separate static compressions to high pressures. Initially, we conducted two static compressions up to ~20 GPa with an alcohol mixture (Methanol: Ethanol) as the pressure transmitting medium (PTM). The hydrostatic limit of alcohol mixture is ~10 GPa (Klotz et al. 2009). This was followed by two

125 static compressions up to ~20 GPa with neon (Ne) gas as the PTM. In addition, we also
126 conducted one static compression up to ~60 GPa with Ne as the PTM. The Ne loading was done
127 at the COMPRES facility, GSECARS, Advanced Photon Source, Argonne National Laboratory
128 (Supporting Table ST1). Ne is reported to be hydrostatic up to ~15 GPa (Klotz et al. 2009).
129 However, the pressure gradient due to non-hydrostaticity is negligible and the PTM remains
130 quasi-hydrostatic to very high pressures (Fei et al. 2007; Klotz et al. 2009). We compressed the
131 sample to pressures beyond the hydrostatic limit of the alcohol mixture, ~10 GPa (Klotz et al.
132 2009). This enables us to get insight into the comparative difference between the two PTM i.e.,
133 alcohol mixture and Ne gas. We used ruby fluorescence for determining the pressure within the
134 symmetric DAC (Mao et al. 1986).

135 We have supplemented our Raman experiments with first-principles simulations based on
136 the density functional theory (DFT) (Hohenberg and Kohn 1964; Kohn and Sham 1965). We
137 employed a widely used approximation to the exchange-correlation functional: the generalized
138 gradient approximation (GGA) (Perdew and Yue 1986; Perdew 1991; Perdew et al. 1996). We
139 have used the highly accurate projector augmented wave method (PAW) (Kresse and Joubert
140 1999) as implemented in the Vienna *ab initio* simulation package (VASP) (Kresse and Hafner
141 1993; Kresse and Furthmüller 1996a, 1996b; Kresse and Joubert 1999). We used the crystal
142 structure of 3.65 Å phase refined at the ambient condition from prior studies (Wunder et al.
143 2011; Welch and Wunder 2012) as a starting guess for the first-principles simulations. We
144 performed a static first-principles simulation on the primitive unit cell of 3.65 Å phase with a $P2_1$
145 space group with 28 atoms in the unit cell. We used an energy cut-off E_{cut} = 800 eV and a
146 Monkhorst-Pack (Monkhorst and Pack 1976) 4×4×3 k-point mesh, yielding 21 k points in the
147 irreducible wedge of the Brillouin zone. A series of convergence tests demonstrated that these

computational parameters yield total energies that are converged within 5 meV/atom. In contrast to a recent study that focused on the determination of the equation of state using energy vs. volume relationship and pressure dependence of elasticity (Mookherjee et al. 2015), in this study, our goal is to predict vibrational modes under ambient conditions. Hence, for calculating vibrational modes, we used a python based pre-and post-processing code- PHONOPY (Togo and Tanaka 2015) in conjunction with the DFT code VASP. We used an experimentally determined zero pressure unit cell volume of 194.52 $Å^3$ and created a $2\times2\times2$ supercell with 224 atoms and determined the vibrational modes.

RESULTS

The Raman spectra of the 3.65 Å phase are better understood in terms of its crystal structure that has a $P2_1$ space group symmetry. The crystal structure of the 3.65 Å phase consists of alternating MgO_6 and SiO_6 octahedral units that are corner shared. In addition, the hydrogen atoms are bonded to the oxygen atoms to form chains of the hydrogen-bonded network (Figure 1) (Wunder et al. 2011; Kleppe et al. 2012; Welch and Wunder 2012; Mookherjee et al. 2015). The unit cell of the 3.65 Å phase consists of two formula units (Z= 2) i.e., 28 total atoms (Figure 1). With three degrees of freedom, the total expected vibrational modes are 84 (42A+ 42B). However, three of these modes are acoustic modes (1A+ 2B). Thus the total number of optic modes is 81 (41A+ 40B) and all these 81 modes are Raman active. The ambient Raman spectra in the lattice region (180-1200 cm^{-1}) and hydroxyl region (2850-3600 cm^{-1}) are compared with the theoretically predicted Raman spectra. Overall the experimentally observed modes are in good agreement with the predicted modes (Figure 2). However, in the hydroxyl region, the theoretical predictions are slightly lower in energies compared to the experimental results. This was also observed in a recent comparison between experimental and theoretical predictions

(Borodina et al. 2020). The experimentally observed Raman spectra show a total of 22 modes in the lattice region and six modes in the hydroxyl region i.e., 28 vibrational modes are observed instead of the expected 81 modes. These could be attributed to low scattering cross-sections of several of the predicted modes which are often not detectable. In addition, several of the predicted modes have vibrational energies that are often too close to be resolved in experimental observations. In agreement with the recent study, the 3.65 Å phase's low energy region is characterized by MgO_6 and SiO_6 octahedral deformation coupled with translation and libration modes, octahedral stretching or breathing modes, deformation or bending modes associated with the OH, and bending mode associated with the bridging Mg-O-Si units (Borodina et al. 2020) (Figure 2). In the energy region between 100 and 300 cm^{-1}, we observe several vibrational modes including intense modes at ~ 194 cm^{-1}; 262 cm^{-1}; 268 cm^{-1}; and 285 cm^{-1}. The vibrational mode at 262 cm^{-1} is likely due to the libration of the SiO_6 octahedra. The vibrational mode at 268 cm^{-1} is very likely caused by the deformation motion of the corner shared protonated MgO_6 and SiO_6 octahedral units. The vibrational mode at 285 cm^{-1} can be attributed to the $(Si,Mg)O_6$ octahedral deformation and (Mg,O) translational motion (Supporting Figure SF2, Table 1). In the energy region between 400 and 1000 cm^{-1}, we observe an intense vibrational mode at ~681 cm^{-1} which is likely to be related to deformational or collective bending of the OH modes primarily associated with the H1 and H2 protons. This is also coupled with motions related to the Si-O-Mg bridging. In the energy region greater than 1000 cm^{-1}, we observe two weaker modes at 1140 cm^{-1} and 1176 cm^{-1} that are likely due to the OH bending motion.

At the high-energy region 2850-3600 cm^{-1}, i.e., corresponding to the hydroxyl stretching region, we observe six distinct modes at ambient conditions. These six modes are located at 3461 cm^{-1} (ν_2^{OH}), 3402 cm^{-1} (ν_1^{OH}), 3289 cm^{-1} (ν_5^{OH}), 3225 cm^{-1} (ν_6^{OH}), 3204 cm^{-1} (ν_4^{OH}), and 3145

This is the peer-reviewed, final accepted version for American Mineralogist, published by the Mineralogical Society of America.
The published version is subject to change. Cite as Authors (Year) Title. American Mineralogist, in press.
DOI: https://doi.org/10.2138/am-2022-8515. http://www.minsocam.org/

194 cm^{-1} (ν_3^{OH}) (Supporting Figure SF4). Based on the first-principles simulation, twelve O-H
195 stretching modes are predicted for the six distinct protons. This has also been reported in an
196 earlier study (Wunder et al. 2012) (Figure 3, Table 1). Infrared (IR) spectroscopic studies have
197 revealed the presence of six O-H stretching modes at room temperature. It is likely that at high
198 temperatures, owing to the disorder in proton motions or coupled OH motions, the vibrational
199 modes are broadened and overlap such that instead of the twelve predicted modes, vibrational
200 spectra show only six. However, upon cooling to -190 ^{o}C, at least eight hydroxyl modes were
201 observed (Wunder et al. 2011, 2012). In our ambient spectra, the hydroxyl modes at the highest
202 energies i.e., at 3461 cm^{-1} (ν_2^{OH}) and 3402 cm^{-1} (ν_1^{OH}) are likely to be related to the shorter
203 hydroxyl (d_{O-H}) bond lengths and longer hydrogen ($d_{O-H\ldots O}$) bond distances that correlates
204 with relatively weaker hydrogen bonds. The pair of hydroxyl and hydrogen bond lengths are
205 similar for the H1 and H2 protons i.e., d_{O1-H1}~1.024 Å and $d_{H1\ldots O1}$~ 1.937 Å; and
206 d_{O2-H2}~0.928 Å and $d_{H2\ldots O2}$~2.045 Å and hence we assign ν_1^{OH} and ν_2^{OH} modes to O1-H1 and
207 O2-H2 stretching vibrational modes, respectively (Supporting Table ST2). At relatively lower
208 energy region, four additional modes are observed at 3289 cm^{-1} (ν_5^{OH}), 3225 cm^{-1} (ν_6^{OH}), 3204
209 cm^{-1} (ν_4^{OH}), and 3145 cm^{-1} (ν_3^{OH}). Owing to lower energy, these modes are likely related to
210 shorter d_{O-H} bond lengths and longer $d_{H\ldots O}$ hydrogen bond lengths. The lowest energy mode
211 3145 cm^{-1} (ν_3^{OH}) is likely related to stronger hydrogen bonding and is assigned to the
212 d_{O3-H4}~1.059 Å and shorter $d_{H4\ldots O6}$~ 1.698 Å. The bond distances and the assignment of
213 hydroxyl stretching modes are consistent with prior studies (Wunder et al. 2011, 2012;
214 Mookherjee et al. 2015).

215 The pressure dependence of the vibrational modes is adequately described by a second-
216 order polynomial -

This is the peer-reviewed, final accepted version for American Mineralogist, published by the Mineralogical Society of America.
The published version is subject to change. Cite as Authors (Year) Title. American Mineralogist, in press.
DOI: https://doi.org/10.2138/am-2022-8515. http://www.minsocam.org/

$$\nu_i = \nu_{i0} + b_i P + c_i P^2$$

where, ν_{i0} is the mode frequency at ambient pressures, i.e., 0.1 MPa (10^{-4} GPa), b_i and c_i refers to $\frac{d\nu_i}{dP}$ and $\frac{d^2\nu_i}{dP^2}$ respectively (Table 2). The 3.65 Å phase becomes thermodynamically stable around ~9 GPa (Pawley et al. 2011) and the high pressure stability limit of the 3.65 Å phase in a realistic mantle is dictated by the intersection of the subduction geotherms with the thermal stability of 3.65 Å phase, which is pressure insensitive (Pawley et al. 2011). This limits the maximum pressure stability at equilibrium to ~20 GPa (Supporting Figure SF5). Thus, we conducted five distinct compressions: in two static compressions, we used alcohol mixtures as PTM and compressed up to ~20 GPa. In two additional static compressions, we used neon as PTM and compressed up to ~20 GPa. In an additional static compression with neon as PTM, we have explored pressures up to 60 GPa. Although we have explored high-pressure behavior up to ~60 GPa, we have analyzed the pressure dependence of all the modes to 20 GPa, the maximum pressure stability limit at equilibrium for 3.65 Å phase at the realistic mantle temperature (Table 2). Pressure dependence of modes up to the maximum pressure of 60 GPa, i.e., beyond the maximum pressure stability of 3.65 Å phase is presented in Supporting Table ST2. We note that even though the 3.65 Å phase in a realistic mantle will not be thermodynamically stable beyond 20 GPa. In our room-temperature static compression measurements up to ~60 GPa, the 3.65 Å phase is likely to be in a metastable state.

We observe that in the lattice energy region (180-1200 cm^{-1}), vibrational modes persist up to pressures ~60 GPa with most of the modes exhibiting $b_i^{lattice} > 0$ and $c_i^{lattice} < 0$ (Figure 4, Figure 5, Table 2). We do not find any indication of phase transition up to ~60 GPa from the pressure evolution of the deconvoluted modes. In the hydroxyl stretching region the O-H modes

also exhibit pressure-induced changes including significant broadening and red-shift of all the modes, i.e., $b_i^{OH} < 0$ (Figure 6, Table 2). We find the ν_3^{OH} and ν_4^{OH} modes exhibit the most pressure-induced red-shift with b_3^{OH} = -36.64±0.01 cm^{-1}/GPa and b_4^{OH}= -26.00±0.01 cm^{-1}/GPa. At ambient conditions, the ν_3^{OH} and ν_4^{OH} modes are related to the shortest $d_{H\ldots O}$ distance and upon compression, the hydrogen bonding is strengthened which leads to further shortening of the $d_{H\ldots O}$ distance. In contrast to the ν_3^{OH} and ν_4^{OH} modes, the ν_2^{OH} mode is associated with the longest $d_{H\ldots O}$ distance, $d_{H2\ldots O2}$ ~ 2.045 Å, i.e., the weakest hydrogen bonding. As a result, it softens the least with b_2^{OH} = -4.97±0.5 cm^{-1}/GPa (Table 2). Compression beyond 5 GPa results in a drastic reduction of all the mode intensities. We find that at pressures > 5.9 GPa, we are unable to detect the ν_4^{OH} mode. This is followed by the disappearance of the ν_5^{OH} and ν_6^{OH} modes and at pressures > 9.3 GPa we are unable to detect the ν_3^{OH} mode. We note that only the ν_1^{OH} and ν_2^{OH} modes persist beyond 20 GPa and up to the pressure of ~60 GPa. Since we explored pressures beyond the hydrostatic limit of methanol:ethanol mixture, we repeated our study with neon as a PTM. To assess the effects of non-hydrostaticity we have used the full width at half-maxima (FWHM) of the ν_1^{OH} and ν_2^{OH} modes (Supporting Figure SF6). We find good agreement between the distinct experimental runs where samples were loaded with the different PTM. An increase in the stressed-induced width broadening is expected with the methanol:ethanol mixture beyond its hydrostatic limit i.e., ~10 GPa (Angel et al. 2007). In our study, we note mode broadening of $\Gamma_{\nu_1^{OH}}$ and $\Gamma_{\nu_2^{OH}}$a at pressures > 5 GPa and this is likely due to enhanced proton disorder often observed in hydrous minerals at high-pressures (Tsuchiya et al. 2005). Upon compression beyond 30 GPa, we observe a significant increase in the full width of half maxima of the modes. The pressure-induced broadening is accompanied by a decrease in the mode intensity. The ν_1^{OH} and ν_2^{OH} modes were indistinguishable from the baseline at the highest pressures explored i.e.,

55-60 GPa and deconvolution results in significant errorrs in both energy of the modes and the full width of half maxima.

To better understand the relation between the hydroxyl stretching modes, ν_i^{OH} of the 3.65 Å and its pressure derivatives, b_i^{OH}, we compare results from our study with that of other relevant hydrous phases (Figure 7). We note that the pressure derivatives, b_i^{OH} of the hydroxyl modes increase linearly with the mode frequency ν_i^{OH} for most of the hydrous phases including the 3.65 Å phase. For compressible layered hydrous silicate minerals such as serpentine polymorphs, lizardite, antigorite, chrysotile, talc, and 10 Å phase that has softer bulk moduli, exhibit the steepest trends in the b_i^{OH} vs. ν_i^{OH}. Hydrous phases such as the 3.65 Å phase exhibit an intermediate trend in b_i^{OH} vs. ν_i^{OH}. Hydrous phases such as superhydrous phase B, humite group, chondrodite, and norbergite have relatively stiffer bulk moduli and thus exhibit a flatter trend in b_i^{OH} vs. ν_i^{OH}. The dense hydrous phase D shows a slight negative trend in b_i^{OH} vs. ν_i^{OH} with b_i^{OH} remaining mostly insensitive to ν_i^{OH}. The overall correlation of compressibility with b_i^{OH} trend is consistent with the dependency of ν_i^{OH} on $d_{O-H\ldots O}$ distances which change more rapidly with pressure in compressible solids such as micas and hydroxides.

The OH-stretching frequency of the hydrous minerals is sensitive to the interaction of the proton with its environment to second-, third- and even fourth-nearest-neighbors. The ν_i^{OH} is often strongly correlated with hydrogen bond $d_{O-H\ldots O}$ distances (Libowitzky 1999; Goryainov 2012) (Supporting Figure SF7). Longer hydrogen bond distances $d_{O-H\ldots O}$ is often related to stronger and shorter OH bonds with ν_i^{OH} shifted to higher energies. However, upon compression, these longer hydrogen bond distances often undergo shortening which results in enhanced hydrogen bonds and weakening of OH bond and significant red shift of the ν_i^{OH} with $b_i^{OH} < 0$.

This is the peer-reviewed, final accepted version for American Mineralogist, published by the Mineralogical Society of America.
The published version is subject to change. Cite as Authors (Year) Title. American Mineralogist, in press.
DOI: https://doi.org/10.2138/am-2022-8515. http://www.minsocam.org/

283 In 3.65 Å phase, we note that the magnitude of $b_i^{OH} < 0$ increases with decreasing ν_i^{OH}. This
284 likely indicates that the hydrogen bond lengths shorter at higher pressures (Figure 7, Table 2).

285 **DISCUSSIONS**

286 It is well known that hydrous mineral phases play a vital role in transporting water into
287 the deep Earth. To provide a better geophysical constraint on the degree of mantle hydration it is
288 thus crucial to have better constraints on the elastic properties of such hydrous phases. The
289 parameters that influence bulk seismic velocities of mineral aggregates are the modal abundance
290 of the individual mineral phases, the elasticity of individual mineral phases, and the lattice
291 preferred orientation. Thus, detecting the degree of mantle hydration is dependent on the modal
292 abundance, elasticity, and the lattice preferred orientation of the hydrous phase under extreme
293 conditions. While it could be argued that water in the deep mantle is mostly sequestered in
294 nominally anhydrous minerals and thus the modal abundance of the hydrous phase is likely to be
295 relatively low. Evidence of hydrous phase inclusions within diamonds (Wirth et al. 2007;
296 Keppler 2014; Lovett 2014; Pearson et al. 2014) and ice-VII phase indicating potential
297 supercritical aqueous fluid inclusion within diamonds (Tschauner et al. 2018) from subduction
298 zone settings indicate that hydrous phases are indeed present in the deeply subducted slabs and
299 help in transporting water into the deep Earth. Clearly, constraints on all these parameters are
300 poor for many of the hydrous phases that are experimentally found to be stable at high pressures
301 and temperatures relevant to subduction zone conditions. In addition to all these parameters,
302 there is an additional parameter that could further complicate the detection of the degree of
303 mantle hydration and this is related to the fact that most hydrous phases often undergo pressure-
304 induced strengthening of hydrogen bonds and eventually hydrogen-bond symmetrization. Such
305 hydrogen bond symmetrizations have been reported in dense hydrous phases including phase D

306 (Tsuchiya et al. 2002), phase-H (Tsuchiya and Mookherjee 2015), phase-Egg (Mookherjee et al.
307 2019), and δ-AlOOH (Panero and Stixrude 2004; Tsuchiya et al. 2005; Sano-Furukawa et al.
308 2008). Hydrogen bond symmetrization is known to have a significant effect on the elastic moduli
309 of the hydrous phases. Often such pressure-induced hydrogen-bond symmetrization leads to
310 stiffening of bulk and shear moduli such that the hydrous phase becomes indistinguishable from
311 volumetrically abundant nominally anhydrous mantle minerals. Thus pressure-induced
312 hydrogen-bond symmetrization often makes it difficult to detect mantle hydration via bulk
313 seismological observations.

314 First-principles simulations based on density functional theory have predicted
315 symmetrization of hydrogen bond and thus likely stiffening of elasticity for 3.65 Å phase at ~60
316 GPa (Mookherjee et al. 2015). Although the 3.65 Å phase becomes stable at 9.0 GPa, its high-
317 pressure stability limit is poorly constrained (Wunder et al. 2011). It has very limited temperature
318 stability of ~500 ^{o}C, that is insensitive to pressure (Wunder et al. 2011). At pressures
319 corresponding to predicted symmetrization, i.e., 60 GPa, even the coldest geotherm is likely to
320 exceed ~ 500 ^{o}C. Thus the predicted symmetrization of the hydrogen bond for the 3.65 Å phase
321 is likely to exceed its thermodynamic stability. However, DFT-based simulations often fail to
322 adequately address light elements such as hydrogen as recently documented by considering
323 thermal and nuclear quantum effects (Bronstein et al. 2017). Hence, we explored the high-
324 pressure behavior of the OH region using Raman spectroscopy to assess pressure-induced
325 changes in the hydrogen bonds. Ice phases are known to undergo hydrogen-bond symmetrization
326 at high pressures and previous studies on protonated and deuterated ices have revealed a phase
327 transition at 60 GPa identified from a soft-mode-like behavior of the OH- or OD-stretching mode
328 ($b_i^{OH} < 0$) below the transition followed by a positive pressure-dependence ($b_i^{OH} > 0$) above the

329 transition pressure (Goncharov et al. 1996). The shift in the pressure dependence of the
330 stretching mode is generally interpreted as the transformation of the ice-VII phase to a crystal
331 structure with symmetrized hydrogen bonds. In the present study, as predicted from simulations,
332 the hydrogen bond strength enhances under compression up to ~60 GPa i.e., $b_i^{OH} < 0$, however,
333 the pressure evolution of the OH-stretching modes does not reveal any reversal in the pressure
334 dependence. At the highest pressures explored i.e., 55-60 GPa, the ν_1^{OH} and ν_2^{OH} modes were
335 indistinguishable from the baseline and deconvolution of results in significant errors in both
336 energies of the modes and the full width of half maxima. Therefore, till the highest pressures
337 explored in this study, i.e., 60 GPa which is significantly higher than the high-pressure stability
338 of 3.65 Å phase (Supporting Figure SF5, Figure 6), we were unable to validate the predicted
339 hydrogen-bond symmetrization.

340 High-pressure Raman measurements and the pressure dependence of the vibrational
341 modes may provide a valuable constraint on the ratio of bulk moduli to its pressure derivative
342 that might hint toward the behavior of the hydrous phase at greater depth. We have attempted
343 such analysis for the 3.65 Å phase and compared our estimates based on Raman spectroscopy
344 with that of the equation of state studies. The comparisons are in good agreement thus validating
345 the strength of such analysis based on Raman measurements (Table 3). The ratio of bulk
346 modulus and its pressure derivative, $\frac{K_o}{K'_o}$ can be expressed in terms of the vibrational modes at
347 ambient conditions (ν_{i0}), first derivative, (b_i), and second derivative, (c_i) of the pressure
348 dependence of the vibrational modes as:

$$\frac{K_o}{K'_o} = \left(\frac{b_i}{\nu_{i0}} - \frac{2c_i}{b_i}\right)^{-1}$$

This is the peer-reviewed, final accepted version for American Mineralogist, published by the Mineralogical Society of America.
The published version is subject to change. Cite as Authors (Year) Title. American Mineralogist, in press.
DOI: https://doi.org/10.2138/am-2022-8515. http://www.minsocam.org/

where bulk modulus (K_o) is related to ν_{i0} and b_i via the formalism $K_o = \gamma_i \frac{\nu_{i0}}{b_i}$, where γ_i is the Grüneisen parameter (Chopelas 1990; Hofmeister 1991; Liu 2002), and the pressure derivative of the bulk modulus (K'_o) is related to ν_{i0}, b_i, c_i, and γ_i via the formalism $K'_o = \gamma_i \left(1 - \frac{2\nu_{i0}c_i}{b_i^2}\right)$. For the 3.65 Å phase, we find $\frac{K_o}{K'_o} \sim 14.3 \pm 5.5$ GPa (Supporting Table ST4) in agreement with the recent study (Mookherjee et al. 2015) (Figure 8; Table 3). It is to be noted that determining K'_o accurately from the equation of state studies is often challenging because it tends to exhibit a strong negative correlation with the bulk modulus (K_o) in the equation of state. Thus, the above-mentioned approach provides alternate constraints on $\frac{K_o}{K'_o}$ using the pressure dependence of vibrational modes (Table 3). We note that the $\frac{K_o}{K'_o}$ for the normal mantle phases, and nominally anhydrous minerals in the simplified MgO-SiO_2-H_2O (MSH) ternary system are overall greater than the layered hydrous magnesium silicates (LHMS) and dense hydrous magnesium silicates (DHMS) (Table 3). Prior studies on other hydrous phases indicate overall trends that they are more compressible, which is likely to make their detection challenging at greater depths. Further studies on shear elastic moduli and elastic anisotropy are warranted for determining the degree of deep mantle hydration.

IMPLICATIONS

To provide better geophysical limits on the degree of mantle hydration it is important to have good constraints on the elasticity of hydrous mineral phases. Most equation of state studies indicate that hydrous phases that are stable at relatively shallower depths, i.e, layered hydrous phases and hydroxides, often have lower bulk moduli (K_o) compared to that of the major mantle mineral phases. Based on our high-pressure Raman study on 3.65 Å phase, we do not observe any evidence for structural changes associated with the MgO_6 and SiO_6 octahedral framework,

we do observe the strengthening of hydrogen bonds but we were unable to validate the symmetrization of hydrogen bonding up to pressures of 60 GPa. This is beyond the maximum pressure stability of 3.65 Å phase considering equilibrium thermodynamics. It is well known that symmetrization of hydrogen bonding is often associated with further stiffening of elastic parameters. Thus based on our study, we do not anticipate such stiffening at least up to 60 GPa. Another key parameter is the pressure derivative of the bulk moduli (K'_o) that dictates compressibility at greater depths. Although relatively more compressible at lower pressures, hydrous phases and nominally anhydrous phases have greater compressibility than that of anhydrous or dry mantle phases (Jacobsen 2006). Thus, at conditions relevant to the mantle, the bulk moduli of dry mantle phases and hydrous phases may become indistinguishable. In contrast to the layered hydrous phases, the dense hydrous magnesium silicates and similarly structured mineral phases often have stiffer bulk moduli. Although to fully evaluate the degree of mantle hydration, better constraints on both bulk and shear moduli are needed, often the first step is to constrain the fundamental elastic moduli using the equation of state studies. For hydrous phases that are synthesized using high-pressure experiments, such data may or may not be available.

Acknowledgment

The authors thank an anonymous reviewer, Dr. Mark Welch, and the associate editor Dr. Susannah Dorfman for their constructive criticism which was extremely helpful in adding clarity. This work is funded by the National Science Foundation (NSF) (EAR 1753125 and 1638752). A.B. acknowledges the Dean's Postdoctoral Scholar Fellowship from the College of Arts and Sciences, Florida State University.

Figure Captions

Figure 1: Crystal structure of 3.65 Å phase projected down *b*-axis, i.e., showing the *a*-*c* plane. The crystal structure of the 3.65 Å phase consists of alternating Mg- (beige) and Si- (light green) octahedral units that share corners. All the corner O atoms (red) are attached to H atoms (pink) which form six distinct pairs of hydrogen bonding (dashed lines).

Figure 2: Ambient Raman spectra of the 3.65 Å phase in the low wavenumber and hydroxyl stretching region. The theoretically predicted modes A and B are shown as blue and red dash, respectively. The eigenvectors of the atomic vibrations for selective modes are indicated in the inset.

Figure 3: Hydrogen bond configurations: O1-H1…O1 is seen in the *a*-*b* plane i.e., projection down the *c*-axis; O2-H2…O2 is seen in the *b*-*c* plane, i.e., projection down the *a*-axis; O4-H3…O5, O3-H4…O6, O5-H5…O3, and O6-H6…O4 form a crank-shaft arrangement that is seen in the *a*-*c* plane, i.e., projection down the *b*-axis; similarly, the crank-shaft arrangement is also seen in the *b*-*c* plane, i.e., projection down the *a*-axis.

Figure 4: (a) Pressure-dependent Raman spectra of the low wavenumber region ~150-1250 cm^{-1} of the 3.65 Å phase. (b) Pressure-dependent Raman spectra of the hydroxyl stretching region ~2850 -3550 cm^{-1} of the 3.65 Å phase.

Figure 5: Pressure dependence of the vibrational mode frequencies of the 3.65 Å phase in the low energy region. Deconvoluted mode frequencies from five compressional runs using two different pressure media are overlain. The pressure dependence of the modes is adequately described by a polynomial expression shown as a dashed line. The fit parameters ν_{i0}, b_i, and c_i, within the high-pressure stability limit (Supporting Figure SF5) i.e., for pressure dependence up to 20 GPa is reported in Table 2. The fit parameters ν_{i0}, b_i, and c_i, beyond the high-pressure

stability limit (Supporting Figure SF5) i.e., for pressure dependence up to 60 GPa is reported in Supporting Table ST3.

Figure 6: (a) Plot of the pressure dependence of the vibrational mode frequencies of the 3.65 Å phase in the hydroxyl stretching region. Deconvoluted mode frequencies from five compressional runs using two different PTM. The pressure dependence of the modes is adequately described by a polynomial expression shown as a dashed line. The fit parameters ν_{i0}, b_i, and c_i, within the high-pressure stability limit (Supporting Figure SF5) i.e., for pressure dependence up to 20 GPa is reported in Table 2. The fit parameters ν_{i0}, b_i, and c_i, beyond the high-pressure stability limit (Supporting Figure SF5) i.e., for pressure dependence up to 60 GPa is reported in Supporting Table ST3. The shaded regions indicate the stability of the 3.65 Å phase (blue gradient), the predicted hydrogen bond symmetrization (pink), upper mantle (UM: light green gradient), mantle transition zone (MTZ: blue), and lower mantle (LM: dark green gradient). (b) The 3.65 Å phase forms at around ~9 GPa (Pawley et al. 2011). The 3.65 Å phase is not thermodynamically stable below 9 GPa (Pawley et al. 2011). The high pressure stability limit of 3.65 Å phase in a realistic mantle is dictated by the intersection of the subduction geotherms with the thermal stability of 3.65 Å phase, which is pressure insensitive (Pawley et al. 2011). The thermodynamic stability region of the 3.65 Å phase is indicated by a shaded region (blue gradient). The solid dark gray line indicates the water-ice VII phase boundary. The solid light gray line indicates Tonga slab geotherm (Syracuse et al. 2010). The dashed lines indicate the lowest temperature predicted in the Tonga slab (Bina and Navrotsky 2000).

Figure 7: The pressure dependence of hydroxyl stretching mode frequency, b_i^{OH} with OH-stretching mode frequency, ν_i^{OH} at ambient condition, i.e., 1 bar, for different hydrous mineral phases in the MSH ternary system. Reference for mineral phases: Chondrodite – (Liu et al.

2003); Clinohumite – (Liu et al. 2003, 2021); Humite – (Liu et al. 2021); Norbergite – (Liu et al. 2021); 10 Å – (Comodi et al. 2007; Parry et al. 2007); Superhydrous B – (Koch-Müller et al. 2005); Phase D – (Shieh et al. 2009); Phase E – (Kleppe et al. 2001); Serpentine: Antigorite – (Auzende et al. 2004; Noguchi et al. 2012); Serpentine: Chrysotile – (Auzende et al. 2004); Serpentine: Lizardite – (Auzende et al. 2004); Talc – (Scott et al. 2007); Ice VII – (Hsieh and Chien 2015); Cummingtonite – (Yang et al. 1998).

Figure 8: The plot shows a systematic relation between the ratio of bulk moduli, K_o to its pressure derivative, K'_o i.e., $\left(\frac{K_o}{K'_o}\right)$ and density (ρ) systematics for various hydrous mineral phases in MSH ternary system. The $\left(\frac{K_o}{K'_o}\right)$ and density data (ρ) for the mineral phases are colored based on their water content. The systematic relation is best described by a power function shown in by gray dashed line $\left(\frac{K_o}{K'_o}\right) = \left(\frac{K_o}{K'_o}\right)_o + A\rho^n$, where, $\left(\frac{K_o}{K'_o}\right)_o$ ~-1.8114±13.0, A~0.45716 ±1.08, and n ~3.5491±1.62. The confidence band is shown in light blue shading. The filled sphere represents data from X-ray diffraction (Table 3). The filled rhomb represents $\left(\frac{K_o}{K'_o}\right)$ for 3.65 Å phase deduced from pressure dependence of Raman data (this study; Supporting Table ST4). The darker symbols represent lower or no water content whereas lighter symbols represent mineral phases that are richer in H_2O wt %. The horizontal color scale shows the H_2O wt%. The color scale helps to distinguish the dry, nominally anhydrous, and hydrous phases. The symbol sizes are also proportional to water content i.e., the darker symbols are smaller in size, and lighter symbols are larger in size. The ternary diagram (in mol%) modified from (Wunder et al. 2012; Mookherjee et al. 2015) is also shown with various hydrous phases in the MgO-SiO_2-H_2O (MSH) system, including 3.65 Å phase. Mineral abbreviations and stoichiometry: br = brucite [$Mg(OH)_2$], tlc = talc [$Mg_3Si_4O_{10}(OH)_2$]; 10 Å = 10 Å phase [$Mg_3Si_4O_{10}(OH)_2 \cdot H_2O$], 3.65 Å =

461 3.65 Å phase [$MgSi(OH)_6$], clinohum = clinohumite [$Mg_9Si_4O_{16}(OH)_2$], chond = chondrodite
462 [$Mg_5Si_2O_8(OH)_2$], phA = phase A [$Mg_7Si_2O_8(OH)_6$], phB = phase B [$Mg_{12}Si_4O_{19}(OH)_2$], phH =
463 phase H [$MgSiO_4H_2$] phD = phase D [$MgSi_2H_2O_6$], phE = phase E [$Mg_{2.23}Si_{1.81}H_{2.8}O_6$], cen =
464 clinoenstatite [$MgSiO_3$], mj = majorite [$MgSiO_3$], pv = bridgmanite/perovskite [$MgSiO_3$], ol =
465 olivine [Mg_2SiO_4], wad = wadsleyite [β-Mg_2SiO_4], ri = ringwoodite [γ-Mg_2SiO_4], ser =
466 serpentine [$Mg_3Si_2O_5(OH)_4$], and ShyB = superhydrous phase B [$Mg_{10}Si_3O_{10}(OH)_4$].

References

Angel, R.J., Bujak, M., Zhao, J., Gatta, G.D., and Jacobsen, S.D. (2007) Effective hydrostatic limits of pressure media for high-pressure crystallographic studies. Journal of Applied Crystallography, 40, 26–32.

Auzende, A.-L., Daniel, I., Reynard, B., Lemaire, C., and Guyot, F. (2004) High-pressure behaviour of serpentine minerals: a Raman spectroscopic study. Physics and Chemistry of Minerals, 31, 269–277.

Basu, A., and Mookherjee, M. (2021) Intercalation of Water in Kaolinite ($Al_2Si_2O_5(OH)_4$) at Subduction Zone Conditions: Insights from Raman Spectroscopy. ACS Earth and Space Chemistry, 5, 834–848.

Bezacier, L., Reynard, B., Cardon, H., Montagnac, G., and Bass, J.D. (2013) High-pressure elasticity of serpentine and seismic properties of the hydrated mantle wedge. Journal of Geophysical Research: Solid Earth, 118, 527–535.

Bina, C.R., and Navrotsky, A. (2000) Possible presence of high-pressure ice in cold subducting slabs. Nature, 408, 844–847.

Borodina, U., Goryainov, S., Oreshonkov, A., Shatskiy, A., and Rashchenko, S. (2020) Raman study of 3.65 Å-phase MgSi(OH)6 under high pressure and the bands assignment. High Pressure Research, 40, 495–510.

Bronstein, Y., Depondt, P., and Finocchi, F. (2017) Thermal and nuclear quantum effects in the hydrogen bond dynamical symmetrization phase transition of δ-AlOOH. European Journal of Mineralogy, 29, 385–395.

Chopelas, A. (1990) Thermal properties of forsterite at mantle pressures derived from vibrational spectroscopy. Physics and Chemistry of Minerals, 17, 149–156.

490 Comodi, P., Cera, F., Dubrovinsky, L., and Nazzareni, S. (2006) The high-pressure behaviour of
491 the 10 Å phase: A spectroscopic and diffractometric study up to 42 GPa. Earth and
492 Planetary Science Letters, 246, 444–457.
493 Comodi, P., Cera, F., Nazzareni, S., and Dubrovinsky, L. (2007) Raman spectroscopy of the 10
494 Å phase at simultaneously HP-HT. European Journal of Mineralogy, 19, 623–629.
495 Downs, R.T., Zha, C.S., Duffy, T.S., and Finger, L.W. (1996) The equation of state of forsterite
496 to 17.2 GPa and effects of pressure media. American Mineralogist, 81, 51–55.
497 Fei, Y., Ricolleau, A., Frank, M., Mibe, K., Shen, G., and Prakapenka, V. (2007) Toward an
498 internally consistent pressure scale. Proceedings of the National Academy of Sciences, 104,
499 9182–9186.
500 Finger, L.W., Ko, J., Hazen, R.M., Gasparik, T., Hemley, R.J., Prewitt, C.T., and Weidner, D.J.
501 (1989) Crystal chemistry of phase B and an anhydrous analogue: implications for water
502 storage in the upper mantle. Nature, 341, 140–142.
503 Frost, D.J., and Fei, Y. (1999) Static compression of the hydrous magnesium silicate phase D to
504 30 GPa at room temperature. Physics and Chemistry of Minerals, 26, 415–418.
505 Gerald Pacalo, R.E., and Weidner, D.J. (1996) Elasticity of superhydrous B. Physics and
506 Chemistry of Minerals, 23, 520–525.
507 ——— (1997) Elasticity of majorite, MgSiO3 tetragonal garnet. Physics of the Earth and
508 Planetary Interiors, 99, 145–154.
509 Goncharov, A.F., Struzhkin, V. V., Somayazulu, M.S., Hemley, R.J., and Mao, H.K. (1996)
510 Compression of Ice to 210 Gigapascals: Infrared Evidence for a Symmetric Hydrogen-
511 Bonded Phase. Science, 273, 218–220.
512 Goryainov, S.V. (2012) A model of phase transitions in double-well Morse potential:

513 Application to hydrogen bond. Physica B: Condensed Matter, 407, 4233–4237.
514 Hirschmann, M.M. (2006) Water, Melting, and the Deep Earth H_2O Cycle. Annual Review of
515 Earth and Planetary Sciences, 34, 629–653.
516 Hofmeister, A.M. (1991) Calculation of bulk modulus and its pressure derivatives from
517 vibrational frequencies and mode Grüneisen Parameters: Solids with cubic symmetry or one
518 nearest-neighbor distance. Journal of Geophysical Research, 96, 16181.
519 Hohenberg, P., and Kohn, W. (1964) Inhomogeneous Electron Gas. Physical Review, 136,
520 B864–B871.
521 Hsieh, W.-P., and Chien, Y.-H. (2015) High pressure Raman spectroscopy of H_2O-CH_3OH
522 mixtures. Scientific Reports, 5, 8532.
523 Iwamori, H. (1998) Transportation of H_2O and melting in subduction zones. Earth and Planetary
524 Science Letters, 160, 65–80.
525 ——— (2004) Phase relations of peridotites under H_2O-saturated conditions and ability of
526 subducting plates for transportation of H_2O. Earth and Planetary Science Letters, 227, 57–
527 71.
528 ——— (2007) Transportation of H_2O beneath the Japan arcs and its implications for global
529 water circulation. Chemical Geology, 239, 182–198.
530 Jacobsen, S.D. (2006) Effect of Water on the Equation of State of Nominally Anhydrous
531 Minerals. Reviews in Mineralogy and Geochemistry, 62, 321–342.
532 Jahn, S., Wunder, B., Koch-Müller, M., Tarrieu, L., Pöhle, M., Watenphul, A., and Taran, M.N.
533 (2012) Pressure-induced hydrogen bond symmetrisation in guyanaite, β-CrOOH: evidence
534 from spectroscopy and ab initio simulations. European Journal of Mineralogy, 24, 839–850.
535 Jiang, F., Speziale, S., and Duffy, T.S. (2006) Single-crystal elasticity of brucite, $Mg(OH)_2$, to 15

GPa by Brillouin scattering. American Mineralogist, 91, 1893–1900.

Karato, S. (2010) Rheology of the Earth's mantle: A historical review. Gondwana Research, 18, 17–45.

Kawamoto, T. (2006) Hydrous Phases and Water Transport in the Subducting Slab. Reviews in Mineralogy and Geochemistry, 62, 273–289.

Keppler, H. (2014) Earth's deep water reservoir. Nature, 507, 174–175.

Kleppe, A.K., Jephcoat, A.P., and Ross, N.L. (2001) Raman spectroscopic studies of phase E to 19 GPa. American Mineralogist, 86, 1275–1281.

Kleppe, A.K., Welch, M.D., Crichton, W.A., and Jephcoat, A.P. (2012) Phase transitions in hydroxide perovskites: a Raman spectroscopic study of stottite, $FeGe(OH)_6$, to 21 GPa. Mineralogical Magazine, 76, 949–962.

Klotz, S., Chervin, J.-C., Munsch, P., and Le Marchand, G. (2009) Hydrostatic limits of 11 pressure transmitting media. Journal of Physics D: Applied Physics, 42, 075413.

Koch-Müller, M., Dera, P., Fei, Y., Hellwig, H., Liu, Z., Orman, J. Van, and Wirth, R. (2005) Polymorphic phase transition in Superhydrous Phase B. Physics and Chemistry of Minerals, 32, 349–361.

Koch-Müller, M., Appelt, O., Wunder, B., and Wirth, R. (2021) New insights in the mechanisms of the reaction 3.65 Å phase = clinoenstatite + water down to nanoscales. European Journal of Mineralogy, 33, 675–686.

Kohn, W., and Sham, L.J. (1965) Self-Consistent Equations Including Exchange and Correlation Effects. Physical Review, 140, A1133–A1138.

Kresse, G., and Furthmüller, J. (1996a) Efficiency of ab-initio total energy calculations for metals and semiconductors using a plane-wave basis set. Computational Materials Science,

559 6, 15–50.
560 ——— (1996b) Efficient iterative schemes for ab initio total-energy calculations using a plane-
561 wave basis set. Physical Review B, 54, 11169–11186.
562 Kresse, G., and Hafner, J. (1993) Ab initio molecular dynamics for liquid metals. Physical
563 Review B, 47, 558–561.
564 Kresse, G., and Joubert, D. (1999) From ultrasoft pseudopotentials to the projector augmented-
565 wave method. Physical Review B, 59, 1758–1775.
566 Kudoh, Y., Nagase, T., Sasaki, S., Tanaka, M., and Kanzaki, M. (1995) Phase F, a new hydrous
567 magnesium silicate synthesized at 1000 ^{o}C and 17 GPa: Crystal structure and estimated bulk
568 modulus. Physics and Chemistry of Minerals, 22, 295–299.
569 Kung, J. (2005) In-situ elasticity measurement for the unquenchable high-pressure clinopyroxene
570 phase: Implication for the upper mantle. Geophysical Research Letters, 32, L01307.
571 Libowitzky, E. (1999) Correlation of O-H stretching frequencies and O-H…O hydrogen bond
572 lengths in minerals. Monatshefte für Chemie / Chemical Monthly, 130, 1047–1059.
573 Liu, D., Smyth, J.R., Zhu, X., Miao, Y., Hu, Y., Chen, G., and Ye, Y. (2021) High-pressure
574 vibrational spectra of humite-group minerals: Fluorine effect on thermodynamic properties
575 and hydrogen bonds. Physics of the Earth and Planetary Interiors, 312, 106654.
576 Liu, L. (2002) Are hydrous phases more compressible? Implications for high-velocity zones in
577 the deep mantle. Geophysical Journal International, 149, 37–43.
578 Liu, Z., Lager, G.A., Hemley, R.J., and Ross, N.L. (2003) Synchrotron infrared spectroscopy of
579 OH-chondrodite and OH-clinohumite at high pressure. American Mineralogist, 88, 1412–
580 1415.
581 Lovett, R.A. (2014) Tiny diamond impurity reveals water riches of deep Earth. Nature.

582 Mao, H.K., Xu, J., and Bell, P.M. (1986) Calibration of the ruby pressure gauge to 800 kbar
583 under quasi-hydrostatic conditions. Journal of Geophysical Research, 91, 4673.
584 Mao, Z., Jacobsen, S.D., Jiang, F., Smyth, J.R., Holl, C.M., and Duffy, T.S. (2008) Elasticity of
585 hydrous wadsleyite to 12 GPa: Implications for Earth's transition zone. Geophysical
586 Research Letters, 35, L21305.
587 Mao, Z., Jacobsen, S.D., Jiang, F., Smyth, J.R., Holl, C.M., Frost, D.J., and Duffy, T.S. (2010)
588 Velocity crossover between hydrous and anhydrous forsterite at high pressures. Earth and
589 Planetary Science Letters, 293, 250–258.
590 Mao, Z., Lin, J.-F., Jacobsen, S.D., Duffy, T.S., Chang, Y.-Y., Smyth, J.R., Frost, D.J., Hauri,
591 E.H., and Prakapenka, V.B. (2012) Sound velocities of hydrous ringwoodite to 16GPa and
592 673K. Earth and Planetary Science Letters, 331–332, 112–119.
593 Monkhorst, H.J., and Pack, J.D. (1976) Special points for Brillouin-zone integrations. Physical
594 Review B, 13, 5188–5192.
595 Mookherjee, M., Speziale, S., Marquardt, H., Jahn, S., Wunder, B., Koch-Müller, M., and
596 Liermann, H.-P. (2015) Equation of state and elasticity of the 3.65 Å phase: Implications for
597 the X-discontinuity. American Mineralogist, 100, 2199–2208.
598 Mookherjee, M., Panero, W.R., Wunder, B., and Jahn, S. (2019) Anomalous elastic behavior of
599 phase egg, $AlSiO_3(OH)$, at high pressures. American Mineralogist, 104, 130–139.
600 Noguchi, N., Moriwaki, T., Ikemoto, Y., and Shinoda, K. (2012) OH group behavior and
601 pressure-induced amorphization of antigorite examined under high pressure and
602 temperature using synchrotron infrared spectroscopy. American Mineralogist, 97, 134–142.
603 Panero, W.R., and Stixrude, L.P. (2004) Hydrogen incorporation in stishovite at high pressure
604 and symmetric hydrogen bonding in δ-AlOOH. Earth and Planetary Science Letters, 221,

421–431.

Parry, S.A., Pawley, A.R., Jones, R.L., and Clark, S.M. (2007) An infrared spectroscopic study of the OH stretching frequencies of talc and 10 Å phase to 10 GPa. American Mineralogist, 92, 525–531.

Pawley, A.R., Clark, S.M., and Chinnery, N.J. (2002) Equation of state measurements of chlorite, pyrophyllite, and talc. American Mineralogist, 87, 1172–1182.

Pawley, A.R., Chinnery, N.J., Clark, S.M., and Walter, M.J. (2011) Experimental study of the dehydration of 10 Å phase, with implications for its H_2O content and stability in subducted lithosphere. Contributions to Mineralogy and Petrology, 162, 1279–1289.

Pearson, D.G., Brenker, F.E., Nestola, F., McNeill, J., Nasdala, L., Hutchison, M.T., Matveev, S., Mather, K., Silversmit, G., Schmitz, S., and others (2014) Hydrous mantle transition zone indicated by ringwoodite included within diamond. Nature, 507, 221–224.

Perdew, J.P. (1991) Generalized gradient approximations for exchange and correlation: A look backward and forward. Physica B: Condensed Matter, 172, 1–6.

Perdew, J.P., and Yue, W. (1986) Accurate and simple density functional for the electronic exchange energy: Generalized gradient approximation. Physical Review B, 33, 8800–8802.

Perdew, J.P., Burke, K., and Ernzerhof, M. (1996) Generalized Gradient Approximation Made Simple. Physical Review Letters, 77, 3865–3868.

Ross, N.L., and Crichton, W.A. (2001) Compression of synthetic hydroxylclinohumite [$Mg_9Si_4O_{16}(OH)_2$] and hydroxylchondrodite [$Mg_5Si_2O_8(OH)_2$]. American Mineralogist, 86, 990–996.

Sanchez-Valle, C., Sinogeikin, S. V., Smyth, J.R., and Bass, J.D. (2008) Sound velocities and elasticity of DHMS phase A to high pressure and implications for seismic velocities and

anisotropy in subducted slabs. Physics of the Earth and Planetary Interiors, 170, 229–239.

Sano-Furukawa, A., Komatsu, K., Vanpeteghem, C.B., and Ohtani, E. (2008) Neutron diffraction study of δ-AlOOD at high pressure and its implication for symmetrization of the hydrogen bond. American Mineralogist, 93, 1558–1567.

Scott, H.P., Liu, Z., Hemley, R.J., and Williams, Q. (2007) High-pressure infrared spectra of talc and lawsonite. American Mineralogist, 92, 1814–1820.

Shieh, S.R., Mao, H., Konzett, J., and Hemley, R.J. (2000) In-situ high pressure X-ray diffraction of phase E to 15 GPa. American Mineralogist, 85, 765–769.

Shieh, S.R., Duffy, T.S., Liu, Z., and Ohtani, E. (2009) High-pressure infrared spectroscopy of the dense hydrous magnesium silicates phase D and phase E. Physics of the Earth and Planetary Interiors, 175, 106–114.

Syracuse, E.M., van Keken, P.E., and Abers, G.A. (2010) The global range of subduction zone thermal models. Physics of the Earth and Planetary Interiors, 183, 73–90.

Tange, Y., Kuwayama, Y., Irifune, T., Funakoshi, K., and Ohishi, Y. (2012) *P-V-T* equation of state of $MgSiO_3$ perovskite based on the MgO pressure scale: A comprehensive reference for mineralogy of the lower mantle. Journal of Geophysical Research: Solid Earth, 117, B06201.

Togo, A., and Tanaka, I. (2015) First principles phonon calculations in materials science. Scripta Materialia, 108, 1–5.

Tschauner, O., Huang, S., Greenberg, E., Prakapenka, V.B., Ma, C., Rossman, G.R., Shen, A.H., Zhang, D., Newville, M., Lanzirotti, A., and others (2018) Ice-VII inclusions in diamonds: Evidence for aqueous fluid in Earth's deep mantle. Science, 359, 1136–1139.

Tsuchiya, J., and Mookherjee, M. (2015) Crystal structure, equation of state and elasticity of

phase H ($MgSiO_4H_2$) at Earth's lower mantle pressures. Scientific Reports, 5, 15534.

Tsuchiya, J., Tsuchiya, T., Tsuneyuki, S., and Yamanaka, T. (2002) First principles calculation of a high-pressure hydrous phase, δ-AlOOH. Geophysical Research Letters, 29, 15-1-15–4.

Tsuchiya, J., Tsuchiya, T., and Tsuneyuki, S. (2005) First-principles study of hydrogen bond symmetrization of phase D under high pressure. American Mineralogist, 90, 44–49.

Welch, M.D., and Wunder, B. (2012) A single-crystal X-ray diffraction study of the 3.65 Å-phase $MgSi(OH)_6$, a high-pressure hydroxide perovskite. Physics and Chemistry of Minerals, 39, 693–697.

Wirth, R., Vollmer, C., Brenker, F., Matsyuk, S., and Kaminsky, F. (2007) Inclusions of nanocrystalline hydrous aluminium silicate "Phase Egg" in superdeep diamonds from Juina (Mato Grosso State, Brazil). Earth and Planetary Science Letters, 259, 384–399.

Wunder, B., Wirth, R., and Koch-Muller, M. (2011) The 3.65 Å phase in the system MgO-SiO_2-H_2O: Synthesis, composition, and structure. American Mineralogist, 96, 1207–1214.

Wunder, B., Jahn, S., Koch-Müller, M., and Speziale, S. (2012) The 3.65 Å phase, $MgSi(OH)_6$: Structural insights from DFT-calculations and T-dependent IR spectroscopy. American Mineralogist, 97, 1043–1048.

Yagi, T., Mao, H.-K., and Bell, P.M. (1978) Structure and crystal chemistry of perovskite-type $MgSiO_3$. Physics and Chemistry of Minerals, 3, 97–110.

Yang, H., Hazen, R.M., Prewitt, C.T., Finger, L.W., Ren, L., and Hemley, R.J. (1998) High-pressure single-crystal X-ray diffraction and infrared spectroscopic studies of the C2/m-$P2_1/m$ phase transition in cummingtonite. American Mineralogist, 83, 288–299.

674 Table 1: Low wavenumber Raman mode assignments.

	3.65 Å	
	This study	*Borodina (2020)*
Mode Assignment*	ν [cm^{-1}]	
	156 w	
$(Si,Mg)O_6$ rot. + (Si,Mg) tr.	194 w	197
	205 w	
	224 w	
	238 w	
	245 w	
SiO_6 rot.	262 s	265
$(Si,Mg)O_6$ def. + Mg tr.	268 vs	271
$(Si,Mg)O_6$ def. + (Mg,O) tr.	285 s	290
		300
	325 w	
	340 w	
SiO_6 sym. stretch+$(Si,Mg)O_6$ def.	400 w	404
	432 s	
	449 w	
	493 w	
	544 vw	
	562 w	
	644 w	
	668 s	
OH bending+Si-O-Mg bridging	681 vs	681
OH bending		884
OH bending		1036
	1140 w	
	1176 w	

Note: *From Borodina et al. 2020. Abbreviations: rot. -rotation; tr. -translation; def. -deformation; sym. -symmetric; w-weak; vw-very weak; s-strong; vs-very strong.

675

Table 2: Pressure-dependence of the Raman modes of the 3.65 Å phase and expansion coefficients.

	This study						*Borodina [2020]*			
Modes	ν_{i0}	$\sigma\nu_{i0}$	b_i	σb_i	c_i	σc_i	ν_{i0}	b_i	σb_i	
1	198.4	1.0	3.80	0.22	-0.10	0.01	*197*	*5.9*	*0.6*	
2	203.9	0.5	5.48	0.15	-0.06	0.01				
3	226.0	1.1	3.89	0.33	-0.05	0.02				
4	238.5	0.6	4.68	0.28	-0.20	0.03				
5	245.8	0.3	4.11	0.20	-0.07	0.03				
6	264.8	1.1	1.98	0.32	-0.02	0.02	*265*	*2.2*	*0.2*	
7	269.8	17.5	0.80	2.55	0.12	0.09				*Appears at 9.5 GPa*
8	270.3	1.1	5.53	0.28	-0.06	0.01	*271*	*5.2*	*0.5*	
9	288.2	1.0	4.49	0.27	-0.02	0.01	*290*	*4.3*	*0.4*	
10	298.9	1.4	5.60	0.34	-0.09	0.02	*300*	*5*	*0.5*	
11	326.0	0.3	4.52	0.10	-0.06	0.01				
12	340.8	0.5	4.75	0.15	-0.08	0.01				
13	402.3	0.4	2.09	0.10	-0.01	0.01	*404*	*1.9*	*0.2*	
14	432.0	1.2	2.14	0.33	0.02	0.02				
15	446.2	3.3	1.93	0.90	0.09	0.05				
16	470.8	1.1	6.99	0.28	-0.09	0.02				
17	494.3	1.2	6.60	0.41	-0.07	0.02				
18	567.7	2.0	6.88	0.51	-0.06	0.03				
19	664.2	2.8	4.07	0.83	-0.06	0.04				
20	681.4	0.8	5.09	0.21	-0.04	0.01	*681*	*5*	*0.5*	
21	647.5	14.6	7.10	1.35	-0.08	0.03				*Appears at 12 GPa*
							884	*4.1*	*0.4*	
							1036	*3.5*	*0.3*	
22	1140.3	3.1	5.08	0.84	-0.06	0.04				
23	1182.7	2.6	6.58	0.76	-0.04	0.04				
24-OH-3	3144.4	3.0	-36.64	0.01	0.76	0.06	*3147*	*-31.9*	*5.4*	
								-8.6	*5.8*	4.7−6.5 GPa*
25-OH-4	3212.0	3.2	-26.00	0.01	0.52	0.15				
26-OH-6	3230.3	0.2	-9.51	0.10	-0.12	0.01				
27-OH-5	3287.5	2.4	-19.78	0.01	1.68	0.13	*3291*	*-22.5*	*3.8*	
								-2.2	*6*	5.6−6.5 GPa†
28-OH-1	3403.2	0.0	-9.37	0.01	0.06	0.00	*3404*	*-9.3*	*0.9*	
29-OH-2	3458.8	2.0	-4.97	0.50	-0.01	0.00	*3463*	*-5.7*	*0.6*	

Note: Subscript "*i*" refers to the vibrational modes. The pressure dependence of the modes is described by an expansion of the form $\nu_i = \nu_{i0} + b_i P + c_i P^2$ where b_i refers to the first derivative $\frac{\partial \nu_i}{\partial P}$ and c_i refers to the second derivative $\frac{\partial^2 \nu_i}{\partial P^2}$. The ν_{i0} is the mode frequency at P_0 of 1×10^{-4} GPa. Errors represent 1σ uncertainties. The polynomial fit of the pressure dependence of the modes is carried out up to 20 GPa, i.e., within the stability field of 3.65 Å phase. The polynomial fit up to ~60 GPa is provided in the

682 supporting information. Borodina [2020] (Borodina et al. 2020) observed a slope change for ν_3^{OH} mode
683 3147 cm^{-1} at *4.7 GPa and ν_5^{OH} mode 3291 cm^{-1} at †5.6 GPa.

684

685 Table 3: Density, bulk modulus, and water content for various hydrous minerals and phases in the MSH ternary.

Mineral/Phase	Formula	ρ_0 (g/cm3)	K_0 (GPa)	K_0'	$\frac{K_0}{K_0'}$ (GPa)	H_2O (wt%)	Reference
Dense Hydrous Magnesium Silicates (DHMS)							
3.65 Å phase	$MgSi(OH)_6$	2.636	84	4.9	17.1	35	(Mookherjee et al. 2015)

686

687

Clinohumite	$Mg_9Si_4O_{16}(OH)_2$	3.187	119.4	4.8	24.9	2.9	(Ross and Crichton 2001)
Chondrodrite	$Mg_5Si_2O_8(OH)_2$	3.057	115.7	4.9	23.6	5.3	(Ross and Crichton 2001)
Phase A	$Mg_7Si_2O_8(OH)_6$	2.976	106	5.8	18.3	11.84	(Sanchez-Valle et al. 2008)
Phase B	$Mg_{12}Si_4O_{19}(OH)_2$	3.368	163	4.0	40.8	2.43	(Finger et al. 1989); (Kudoh et al. 1995)
Superhydrous phase B	$Mg_{10}Si_3O_{10}(OH)_4$	3.327	154	4.0	38.5	6.49	(Gerald Pacalo and Weidner 1996)
Phase D	$MgSi_2H_2O_6$	3.459	166	4.1	40.5	18.49	(Frost and Fei 1999)
Phase E	$Mg_{2.23}Si_{1.81}H_{2.8}O_6$	2.92	93	5.0	18.6	13.6	(Shieh et al. 2000)
Layered Hydrous Magnesium Silicates (LHMS)							
Brucite	$Mg(OH)_2$	2.38	43.8	6.8	6.4	30.89	(Jiang et al. 2006)
Serpentine	$Mg_3Si_2O_5(OH)_4$	2.62	61	6.7	9.1	13	(Bezacier et al. 2013)
Talc	$Mg_3Si_4O_{10}(OH)_2$	2.75	41	6.0	6.8	4.75	(Pawley et al. 2002)
10 Å phase	$Mg_3Si_4O_{10}(OH)_2.H_2O$	2.676	39	12.5	3.1	9.5	(Comodi et al. 2006)
Mantle phases and nominally anhydrous minerals							
Olivine	Mg_2SiO_4	3.218	125.5	4.0	31.4	0	(Downs et al. 1996)
Clinoenstatite	$MgSiO_3$	3.301	155	5.5	28.2	0	(Kung 2005)
Majorite	$MgSiO_3$	3.522	159.8	5.8	27.6	0	(Gerald Pacalo and Weidner 1997)
Bridgmanite	$MgSiO_3$	4.098	256.7	4.1	62.6	0	(Yagi et al. 1978); (Tange et al. 2012)
Hydrous olivine	Mg_2SiO_4	3.18	125.4	4.5	27.9	0.9	(Mao et al. 2010)
Hydrous wadsleyite	β-Mg_2SiO_4	3.435	161.3	4.1	39.3	0.84	(Mao et al. 2008)
Hydrous ringwoodite	γ-Mg_2SiO_4	3.649	175.2	4.0	43.8	1.1	(Mao et al. 2012)

688

Figure 1

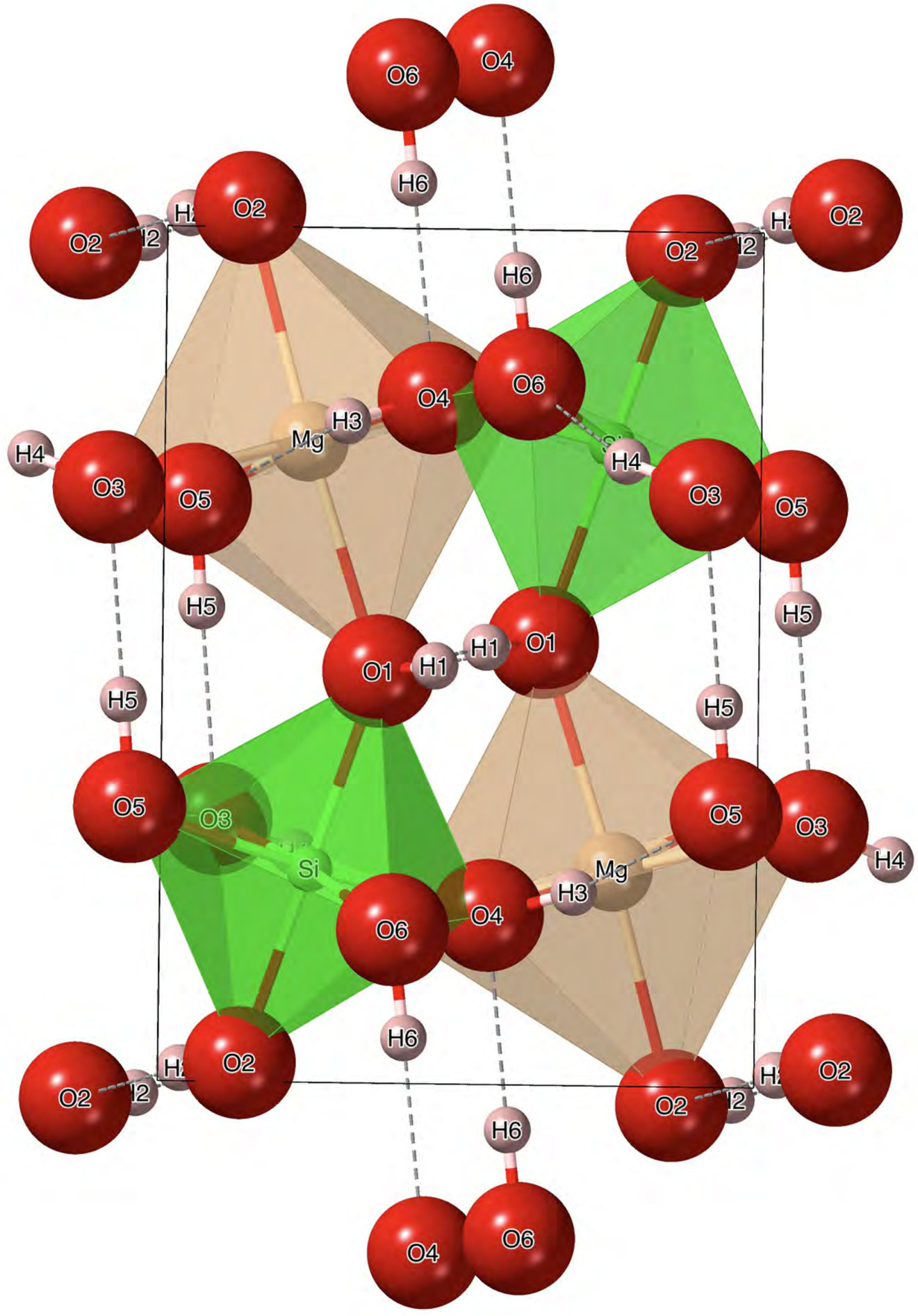

Figure 2

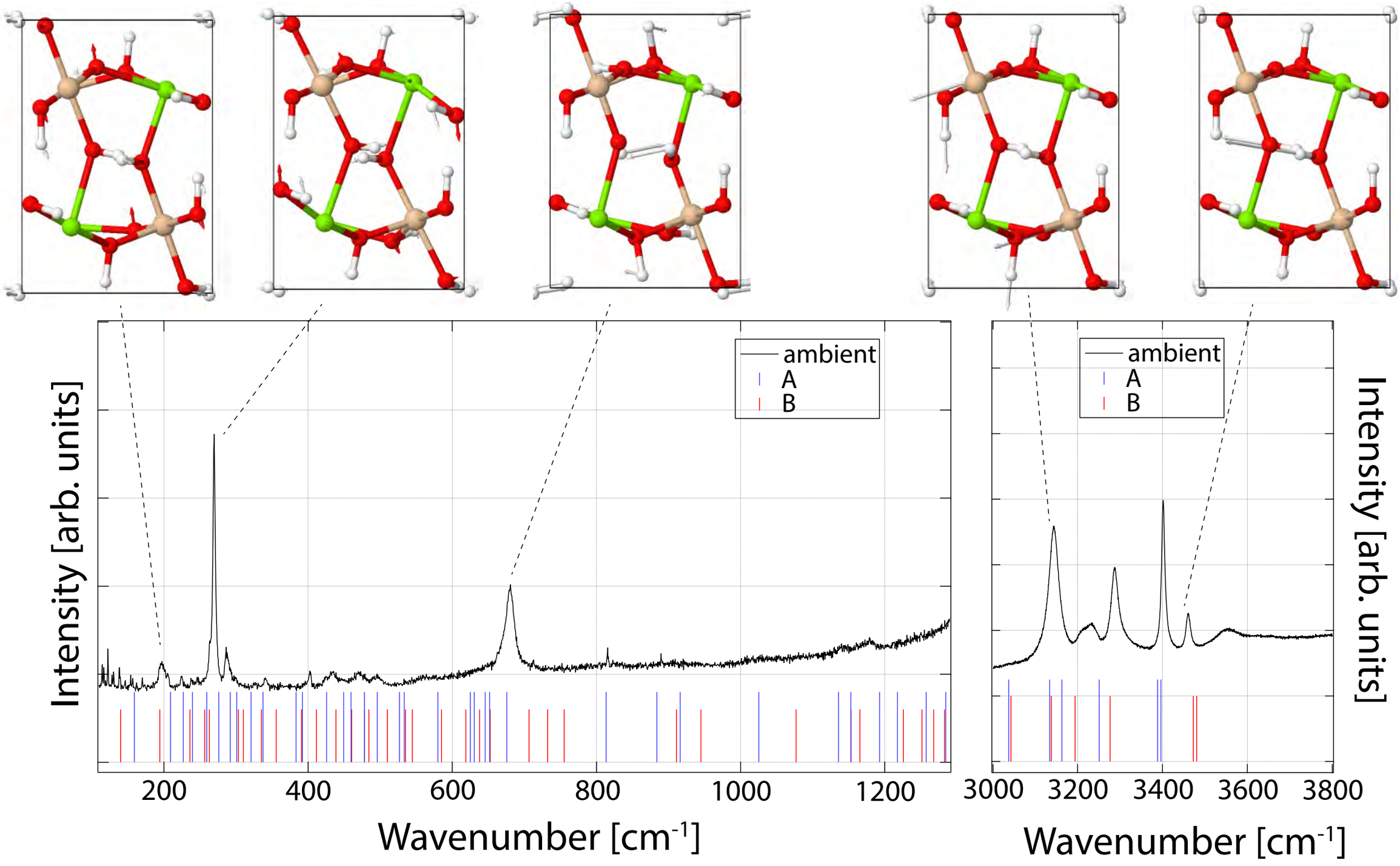
ambient
A
B
Intensity [arb. units]
200
400
600
800
1000
1200
Wavenumber [cm-1]
ambient
A
B
Intensity [arb. units]
3000
3200
3400
3600
3800
Wavenumber [cm-1]

Figure 3

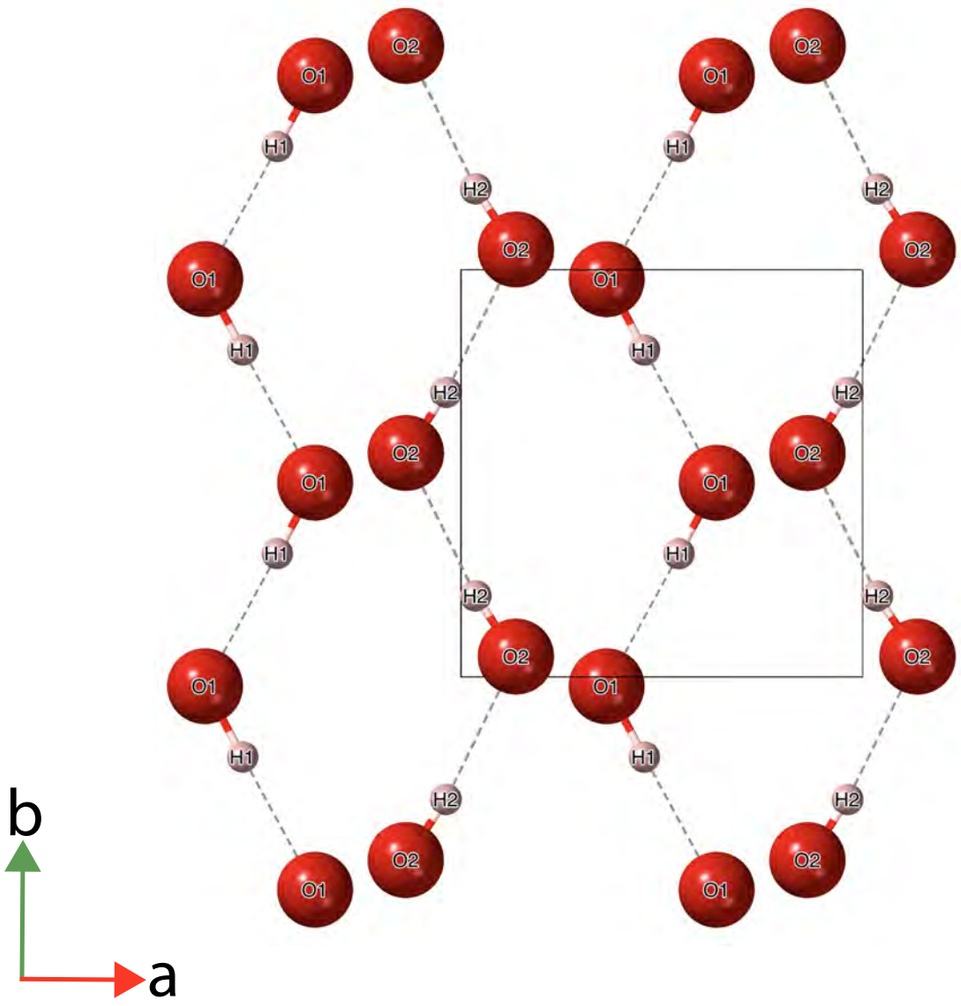
O1
O2
H1
H2
b
a

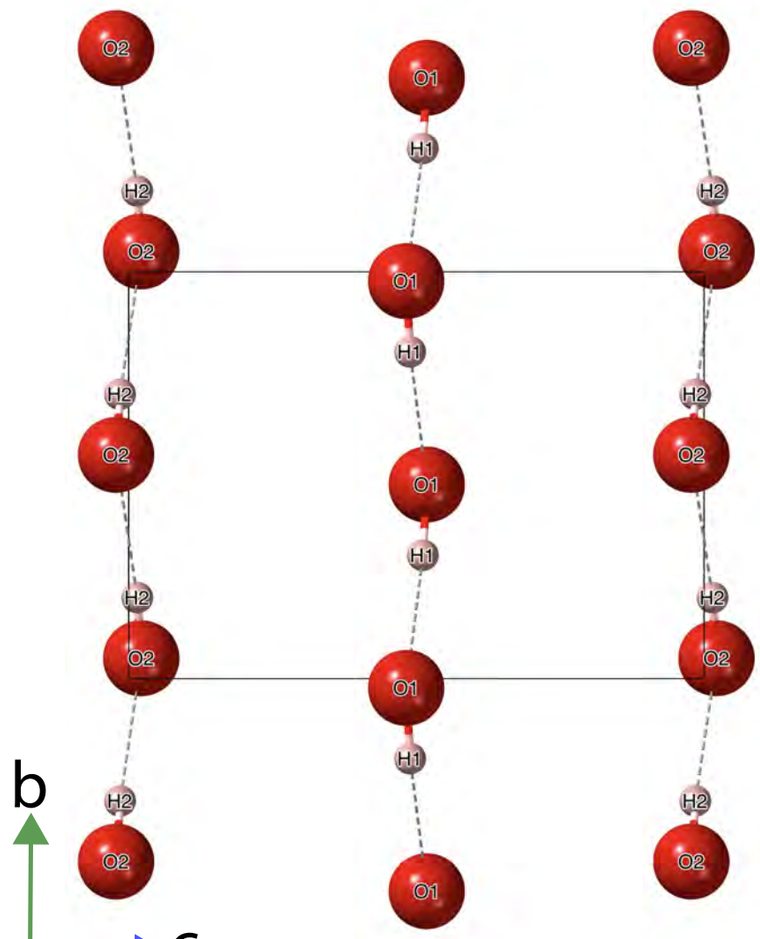
O1
O2
H1
H2
b
c

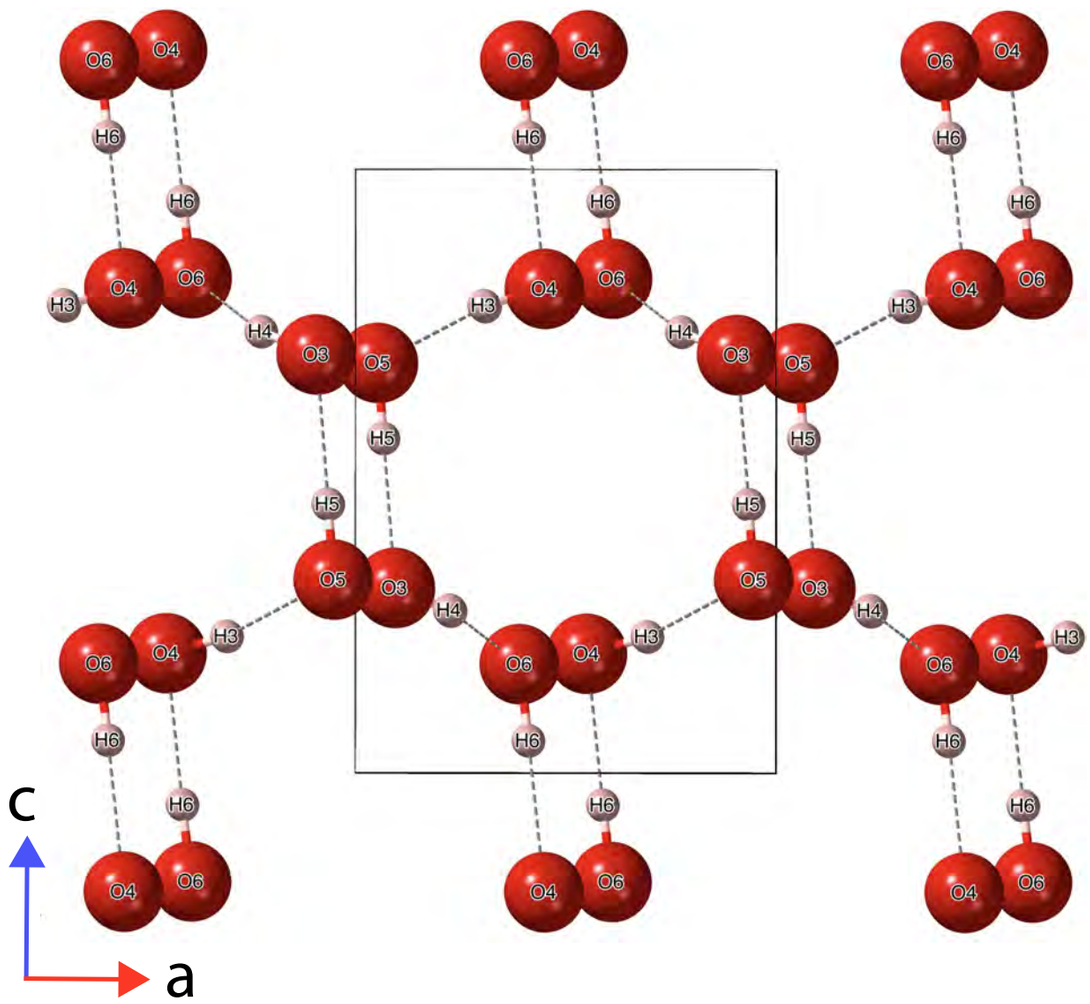
O3
O4
O5
O6
H3
H4
H5
H6
c
a

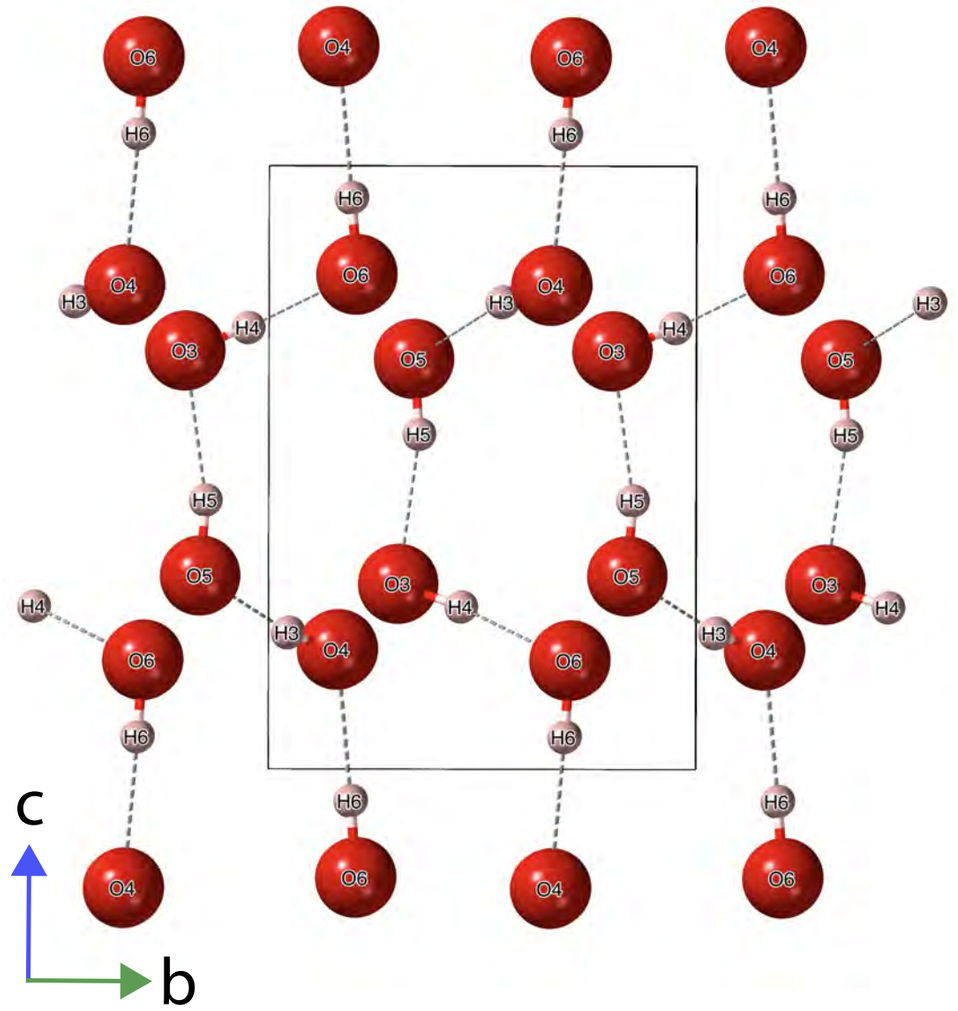
O3
O4
O5
O6
H3
H4
H5
H6
c
b

Figure 4

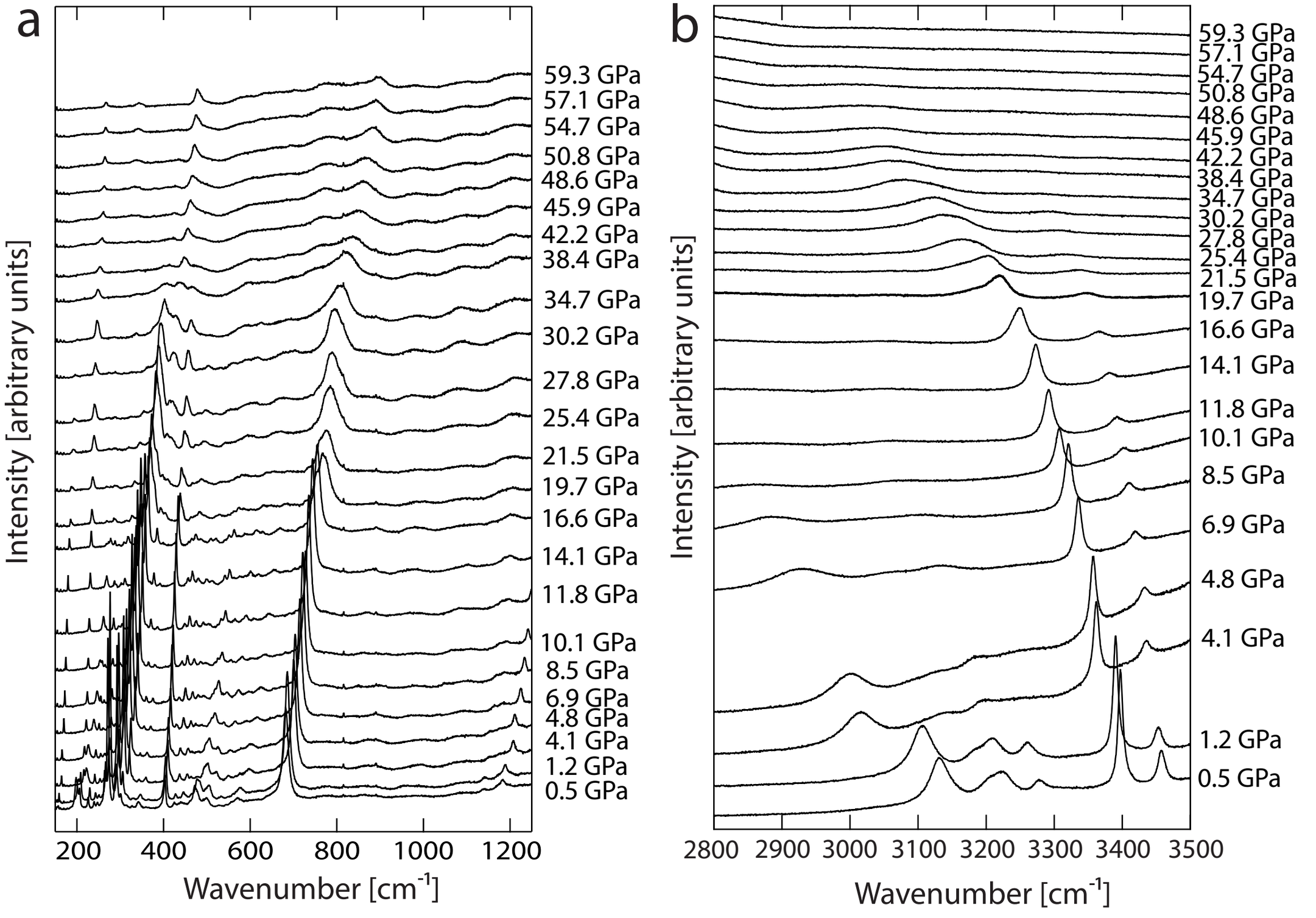
a
Intensity [arbitrary units]
59.3 GPa
57.1 GPa
54.7 GPa
50.8 GPa
48.6 GPa
45.9 GPa
42.2 GPa
38.4 GPa
34.7 GPa
30.2 GPa
27.8 GPa
25.4 GPa
21.5 GPa
19.7 GPa
16.6 GPa
14.1 GPa
11.8 GPa
10.1 GPa
8.5 GPa
6.9 GPa
4.8 GPa
4.1 GPa
1.2 GPa
0.5 GPa
200
400
600
800
1000
1200
Wavenumber [cm-1]
b
Intensity [arbitrary units]
59.3 GPa
57.1 GPa
54.7 GPa
50.8 GPa
48.6 GPa
45.9 GPa
42.2 GPa
38.4 GPa
34.7 GPa
30.2 GPa
27.8 GPa
25.4 GPa
21.5 GPa
19.7 GPa
16.6 GPa
14.1 GPa
11.8 GPa
10.1 GPa
8.5 GPa
6.9 GPa
4.8 GPa
4.1 GPa
1.2 GPa
0.5 GPa
2800
2900
3000
3100
3200
3300
3400
3500
Wavenumber [cm-1]

Figure 5

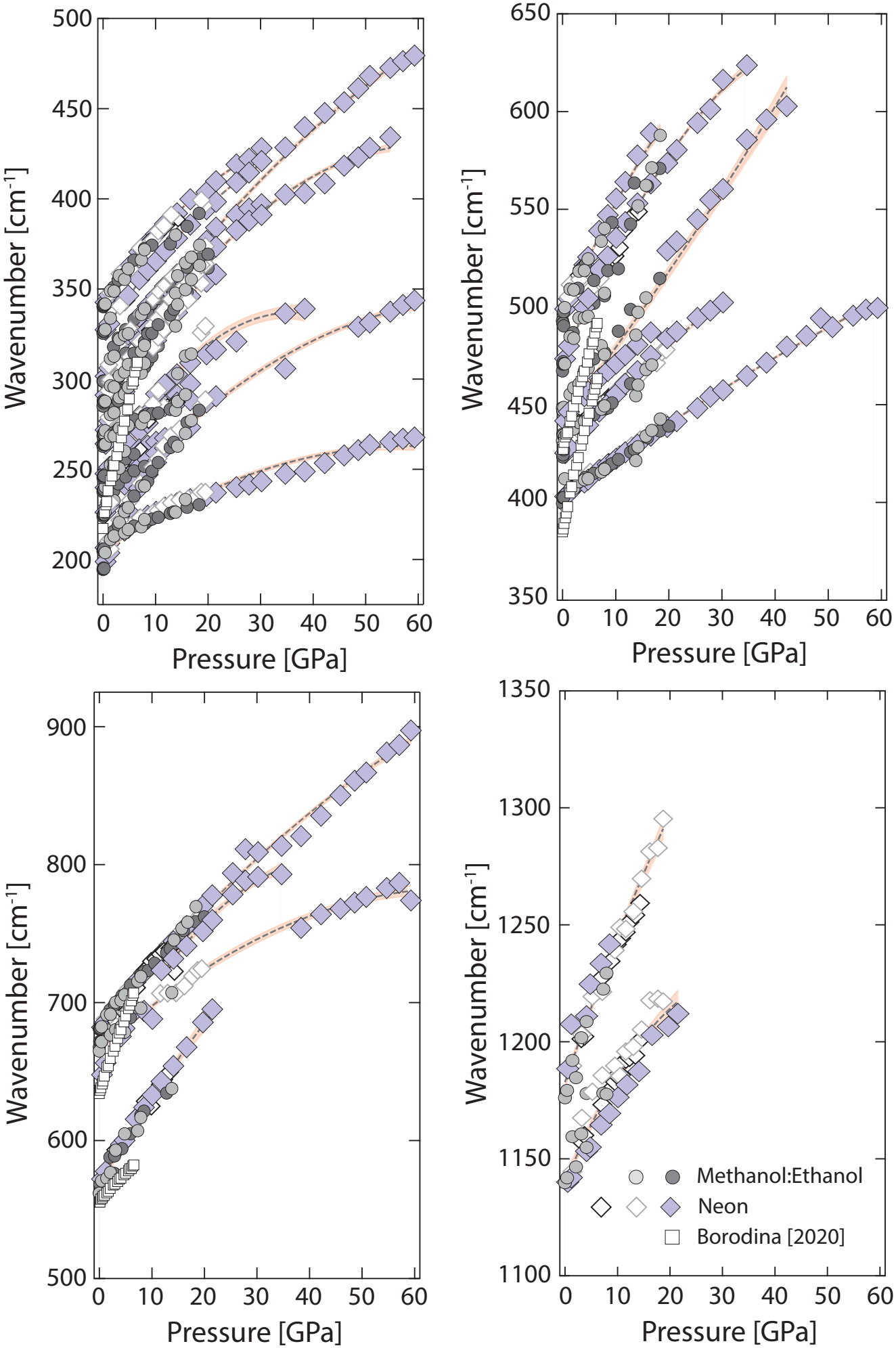
Wavenumber [cm-1]
Pressure [GPa]
Methanol:Ethanol
Neon
Borodina [2020]

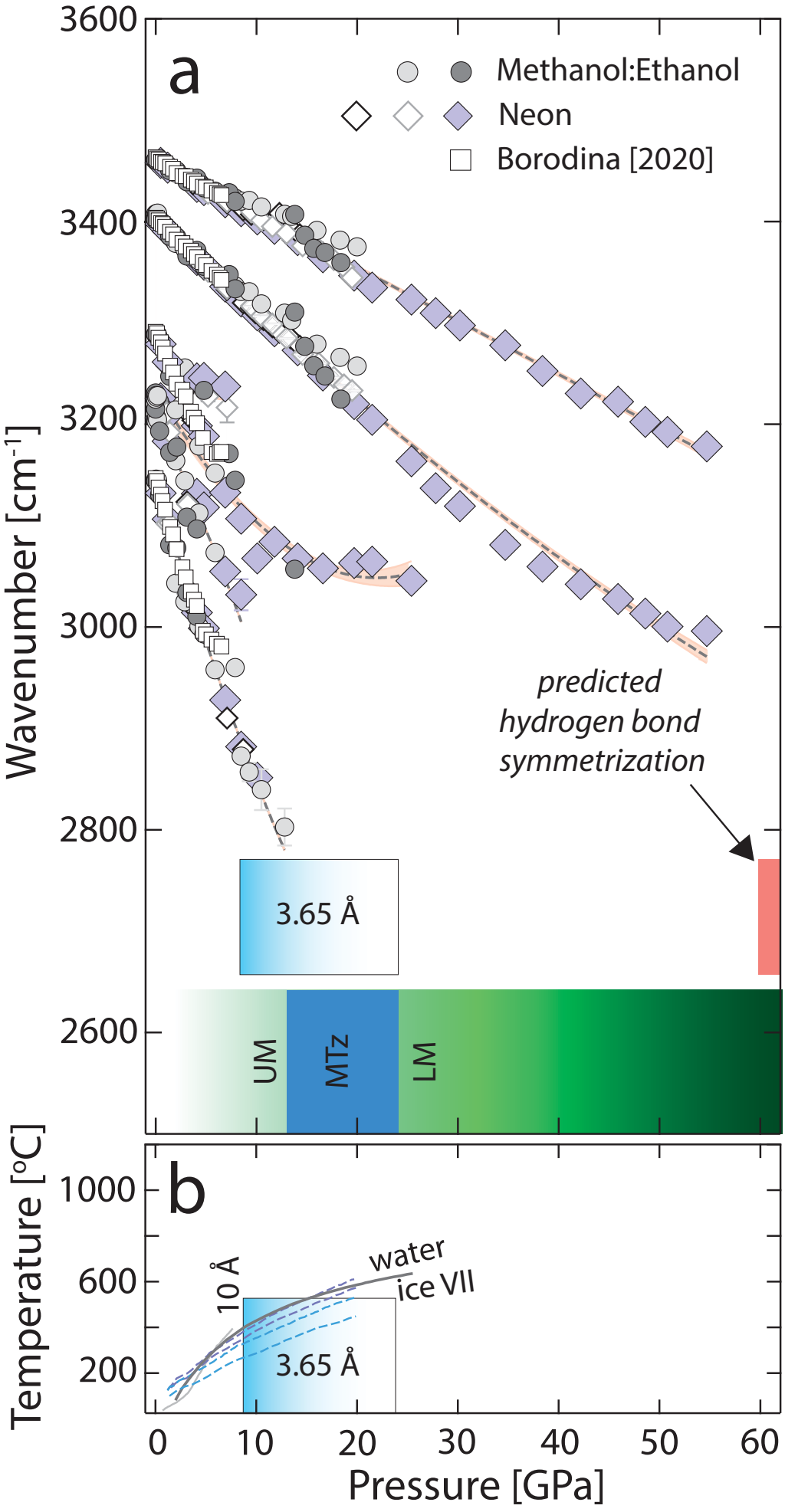
a
Methanol:Ethanol
Neon
Borodina [2020]
predicted
hydrogen bond
symmetrization
3.65 Å
UM
MTz
LM
Wavenumber [cm-1]
3600
3400
3200
3000
2800
2600
b
10 Å
water
ice VII
3.65 Å
Temperature [°C]
1000
600
200
0
10
20
30
40
50
60
Pressure [GPa]

Figure 7

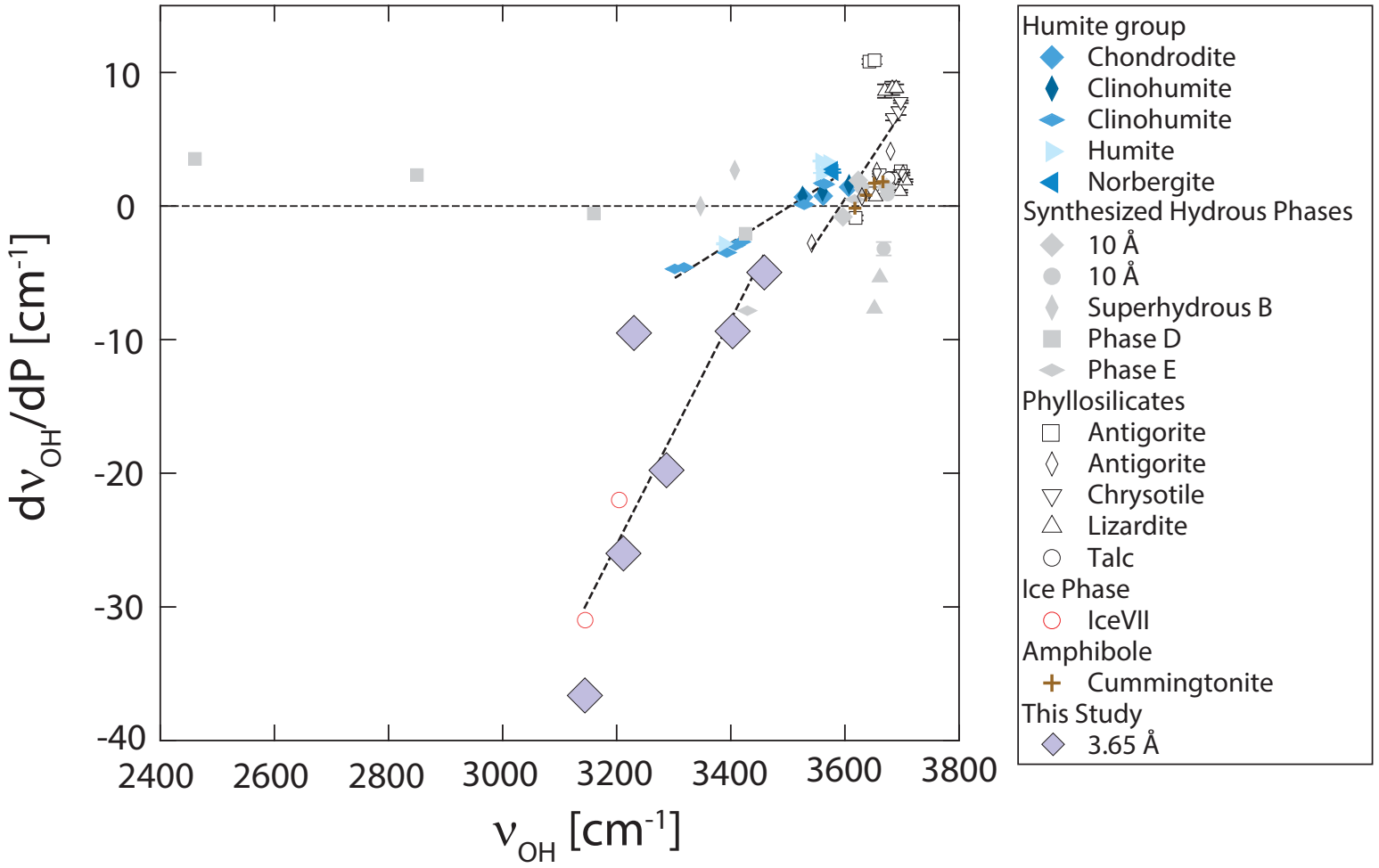
10
0
-10
-20
-30
-40
2400
2600
2800
3000
3200
3400
3600
3800
dν_OH/dP [cm^-1]
ν_OH [cm^-1]
Humite group
Chondrodite
Clinohumite
Clinohumite
Humite
Norbergite
Synthesized Hydrous Phases
10 Å
10 Å
Superhydrous B
Phase D
Phase E
Phyllosilicates
Antigorite
Antigorite
Chrysotile
Lizardite
Talc
Ice Phase
IceVII
Amphibole
Cummingtonite
This Study
3.65 Å

Figure 8

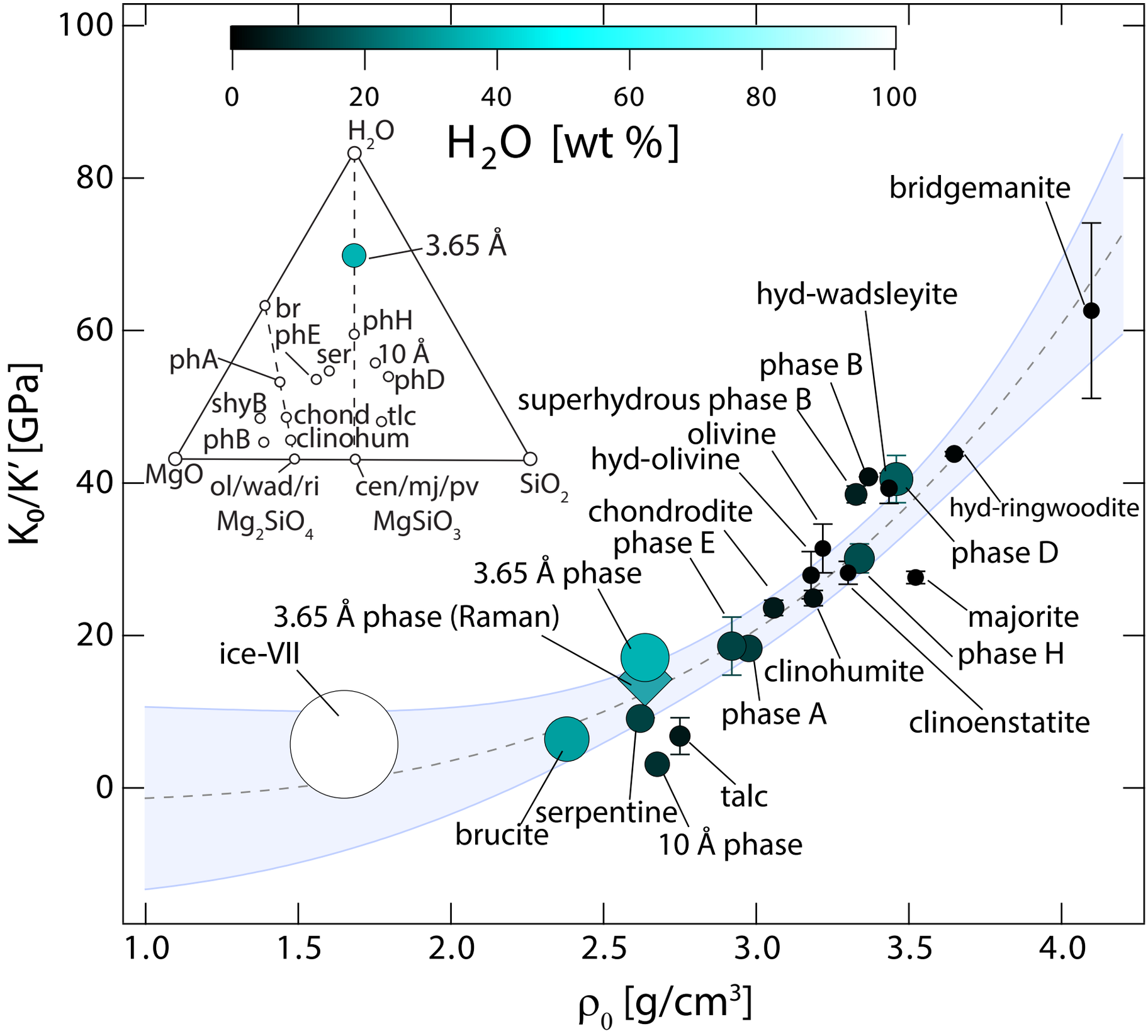
100
80
60
40
20
0
0
20
40
60
80
100
H2O [wt %]
K0/K' [GPa]
1.0
1.5
2.0
2.5
3.0
3.5
4.0
ρ0 [g/cm3]
H2O
3.65 Å
br
phE
phH
phA
ser
10 Å
phD
shyB
chond
tlc
phB
clinohum
MgO
ol/wad/ri
Mg2SiO4
cen/mj/pv
MgSiO3
SiO2
bridgemanite
hyd-wadsleyite
phase B
superhydrous phase B
olivine
hyd-olivine
chondrodite
phase E
3.65 Å phase
3.65 Å phase (Raman)
ice-VII
hyd-ringwoodite
phase D
majorite
phase H
clinohumite
phase A
clinoenstatite
talc
serpentine
brucite
10 Å phase